nature communications

Article

https://doi.org/10.1038/s41467-025-64505-9

Fe-(μ-O)-Zn dual-atom boosting C-C coupling for direct oxidation of methane to acetic acid using O_2

Received: 28 April 2025

Accepted: 17 September 2025

Published online: 27 October 2025

Check for updates

Baiyang Yu[1,2,8], Wenlong Li[3,8], Xuan Tang[3,8], Lu Cheng[3], Jiawei Zhang[1,2], Shuobing Yang[1,2], Fudong Liu[4], Jing Xu[5], Ying Zhang[1,2], Chengsi Pan[1,2], Xiao-Ming Cao[6] ✉, Yongfa Zhu[7] & Yang Lou[1,2] ✉

Direct oxidation of methane (DOM) into high-value C2+ products using molecular oxygen (O_2) is essential for the sustainable production of clean energy and bulk chemicals, but is still challenging due to the difficult C-H activation and uncontrollable C-C coupling process. Herein, we design and construct the Fe-(μ-O)-Zn dual-atom sites by supporting Fe and Zn atoms on ZSM-5 (Fe_1-Zn_1/ZSM-5), which achieves the DOM by O_2 to acetic acid under ambient temperature and pressure. The Fe-(μ-O)-Zn dual-atom sites yield an acetic acid productivity of 3006 μmol•g_{cat}^{-1}•h^{-1} with 86.8% selectivity (total C2+ products selectivity of 93.0%) for at least 20 hours at 25 °C and atmospheric pressure. The mutual electronic modulation between Fe and Zn shifts the *d*-band center of Fe 3*d* in Fe-(μ-O)-Zn dual-atom sites upwards, which promotes the formation and stabilization of highly reactive Fe=O species through O_2 photodissociation and thereby enhances the C-H bond activation of CH_4. The Fe-(μ-O)-Zn dual-atom reaction sites (spatial distance of 2.7 Å) boost the C-C coupling of key CH_3 and HCHO intermediate species, which steadily produce acetic acid and other C2+ oxygenates. This work would broaden the avenue towards the sustainable conversion of methane to value-added C2+ products under ambient temperature and pressure.

As crude oil resources become depleted, catalytic conversion of the naturally abundant methane (CH_4) into high-value products is seen as an important alternative to the oil-based method for the production of energy and chemicals[1], contributing to the establishment of a carbon-neutral society. Compared with traditional C1 products, the conversion of methane to acetic acid (CH_3COOH) and other C2+ products is more attractive[2]. The current industrial process for methane to acetic acid is indirect and energy-intensive, involving methane reforming, methanol synthesis, and subsequent methanol carbonylation[3,4]. Although the direct routes for transforming methane into acetic acid have been explored using both homogeneous and heterogeneous catalysts, the indispensable use of corrosive acid inevitably leads to environmental issues and safety risks[5], which pose great challenges for sustainable development.

Consequently, the direct oxidation of methane (DOM) into acetic acid (CH_3COOH) and other C2+ oxygenates using molecular oxygen

[1]Key Laboratory of Synthetic and Biological Colloids, Ministry of Education, School of Chemical and Material Engineering, Jiangnan University, Wuxi, Jiangsu, China. [2]International Joint Research Center for Photoresponsive Molecules and Materials, Jiangnan University, Wuxi, Jiangsu, China. [3]Centre for Computational Chemistry and Research Institute of Industrial Catalysis, East China University of Science and Technology, Shanghai, China. [4]Department of Chemical and Environmental Engineering, University of California, Riverside, California, USA. [5]School of Food Science and Technology, Jiangnan University, Wuxi, Jiangsu, China. [6]School of Chemistry and Chemical Engineering, Shanghai Jiao Tong University Shanghai, China. [7]Department of Chemistry, Tsinghua University Beijing, China. [8]These authors contributed equally: Baiyang Yu, Wenlong Li, Xuan Tang. ✉e-mail: xmcao@sjtu.edu.cn; yang.lou@jiangnan.edu.cn

(O_2) is of great importance for the sustainable production of clean energy and bulk chemicals[6]. However, the direct synthesis of C2+ products starting from CH_4 often undergoes uncontrollable carbon-carbon coupling mechanisms, making the selectivity for specific products difficult. Furthermore, the direct use of O_2 as an oxidant normally requires harsh conditions, e.g., high temperatures and strong oxidizing atmosphere, to activate oxygen because the cleavage of O_2 to produce surface active oxygen species for CH_4 activation is very difficult[7]. Moreover, the over-oxidation of initially formed oxygenated products into CO_2 and H_2O using the formed surface O* species is thermodynamically favored under the aforementioned harsh conditions, leading to the extremely low yield of value-added oxygenated products[7,8]. Therefore, various efforts have been devoted to the construction of binuclear or trinuclear iron or copper sites confined in zeolites or metal-organic framework (MOF) to mimic the active site structures of methane monooxygenase (MMO) for methane conversion with O_2 under moderate temperatures[9–11]. So far, several catalysts have been reported to drive the CH_4 conversion with O_2 to C1 products at room temperature[1,12], but an artificial process for CH_4 to C2+ products by using O_2 at ambient temperature and pressure remains a great challenge.

Herein, we report that the ZSM-5 supported Fe and Zn dual atoms (Fe_1-Zn_1/ZSM-5) as a concept of proof catalyst not only enable the stable formation of the reactive Fe=O oxygen species via the photodissociation of O_2 under light irradiation at ambient temperature and pressure to efficiently activate C-H bond of methane but also provide dual-atom reaction sites to promote the C-C coupling reaction for DOM to acetic acid and other C2+ oxygenates. As a result, the synthesized Fe_1-Zn_1/ZSM-5 yields a C2+ productivity of 3420 $\mu mol \bullet g_{cat}^{-1} \bullet h^{-1}$ with a C2 + selectivity of 93.0% in all products (acetic acid selectivity of 86.8%) at 25 °C and ambient pressure under light irradiation and sustains the original activity for at least 20 cycles (Supplementary Table S1).

Results

Synthesis and identification of Fe-(μ-O)-Zn reaction sites in Fe_1-Zn_1/ZSM-5

The Fe_1-Zn_1/ZSM-5 catalyst was synthesized via a modified co-adsorption method by finely tuning the adsorption parameters of metal precursors in the aqueous solution under the irradiation of ultraviolet light (details shown in Experimental Section)[13–18]. It has been reported that the introduction of UV light can promote the synthesis of heteronuclear dual-atom catalysts[19–21]. The Si/Al molar ratio of ZSM-5 is 12.5:1, and the actual loadings of Fe and Zn are 0.32 wt.% and 0.34 wt.%, determined by inductively coupled plasma-optical emission spectrometry (ICP-OES). Scanning electron microscope (SEM) back-scatter images indicate no nanoparticles or clusters of Fe and Zn species in Fe_1-Zn_1/ZSM-5, as shown in Supplementary Fig. S1. Furthermore, the TEM images with different magnifications also exhibit that there are no clusters or nanoparticles of Fe and Zn species in Fe_1-Zn_1/ZSM-5 (Supplementary Fig. S2). In addition, no characteristic peaks of Fe or Zn crystal can be observed from the X-ray diffraction pattern (XRD) of Fe_1-Zn_1/ZSM-5 (Supplementary Fig. S3), which further reveals that the Fe and Zn species are highly dispersed on ZSM-5[22,23]. Besides, the HAADF-STEM images exhibit no nanoparticles or clusters of Fe and Zn species observed on Fe_1-Zn_1/ZSM-5 (Supplementary Fig. S4). The mapping results also show that Fe and Zn are evenly dispersed on the ZSM-5 (Supplementary Fig. S5). Additional atomic-scale HAADF-STEM images further verify the diatomic Fe_1-Zn_1 structure, as the average distance between Fe_1-Zn_1 dual atoms is around 2.7 Å (Supplementary Fig. S6 and Supplementary Fig. S7), which is also supported by the extended X-ray absorption fine structure (EXAFS) spectroscopy. Those results further confirm the atomically dispersed state of Fe and Zn species on Fe_1-Zn_1/ZSM-5.

To clarify the local coordination environment of Fe and Zn species in Fe_1-Zn_1/ZSM-5, extended X-ray absorption fine structure (EXAFS) spectroscopy is performed. For the Fe species, there is one Fe-O scattering at 1.5 Å in the first shell of Fe_1-Zn_1/ZSM-5 (Fig. 1a), without any Fe-Fe scattering that will be discussed later in the manuscript, which indicates that the Fe species are atomically dispersed instead of nanoparticles or clusters[24,25]. In addition, the peak at 2.4 Å higher than the Fe-Fe scattering in Fe foil (2.2 $Å^{-1}$) but lower than the Fe-Fe scattering in FeO (2.5 $Å^{-1}$) and Fe_2O_3 (2.5 $Å^{-1}$), can be assigned to the Fe-Zn scattering in the second shell[26], which is further confirmed by the DFT simulation and will be discussed later. This data verifies the presence of Zn species neighboring Fe species. For the Zn species, there is one Zn-O scattering at 1.6 Å in the first shell of Fe_1-Zn_1/ZSM-5 without any Zn-Zn scattering that will be discussed later, as shown in Fig. 1b, which also indicates that the Zn species are atomically dispersed instead of nanoparticles or clusters[25,27]. Besides, the peak at 2.4 Å higher than the Zn-Zn scattering in Zn foil (2.2 Å) but lower than the Zn-Zn scattering in ZnO (2.9 Å) can be assigned to the Zn-Fe scattering in the second shell[26], which is further confirmed by the DFT simulation and will be discussed later. These results confirm the presence of Fe species neighboring Zn species, which is in good agreement with the Fe EXAFS data.

To reveal the local coordination environment of Fe and Zn species in Fe_1-Zn_1/ZSM-5 more clearly, the wavelet transform (WT) of the Fe and Zn K-edge EXAFS oscillations is analyzed. As shown in Fig. 1c, the WT contour plots of Fe atoms in Fe_1-Zn_1/ZSM-5 present one intensity maximum at approximately 4.1 $Å^{-1}$ that can be assigned to the Fe-O coordination, and no intensity maximum related to Fe-Fe coordination can be observed compared with that of the reference Fe foil, FeO, and Fe_2O_3 samples[28]. Meanwhile, due to the scattering effect of Zn on Fe[29,30], there is a weak peak on Fe_1-Zn_1/ZSM-5 at approximately 5.3 $Å^{-1}$, higher than that of Fe-Fe scattering in Fe foil (5.9 $Å^{-1}$), FeO (5.4 $Å^{-1}$), and Fe_2O_3 (6.1 $Å^{-1}$), which can be assigned to the Fe-Zn scattering in WT. In addition, the WT contour plots of Zn species in Fe_1-Zn_1/ZSM-5 present one intensity maximum at approximately 4.2 $Å^{-1}$ that can be assigned to the Zn-O coordination, and no intensity maximum related to Zn-Zn coordination can be observed compared with that of the reference Zn foil and ZnO samples[31,32]. Meanwhile, due to the scattering effect of Fe on Zn[29,30], there is a weak peak on Fe_1-Zn_1/ZSM-5 at 5.4 $Å^{-1}$, lower than that of the Zn-Zn scattering in Zn foil (6.0 $Å^{-1}$) and ZnO (5.7 $Å^{-1}$), which correspondingly can be assigned to Zn-Fe scattering in WT[33,34]. The WT contour plots of Zn species in Fe_1-Zn_1/ZSM-5 are consistent with the Fe spectrum and confirm that the Fe and Zn species exist as paired atoms on Fe_1-Zn_1/ZSM-5.

To accurately reveal the local coordination environment of Fe and Zn species in Fe_1-Zn_1/ZSM-5, various crystal models built by DFT simulation are used to fit the EXAFS data, but only the Z[Fe-(μ-O)-Zn] model fits the original EXAFS data well. Furthermore, the Z[Fe-(μ-O)-Zn] model also fits the original EXAFS data at K-space well (Supplementary Fig. S8), and the fitting details are listed in Supplementary Figs. S9–11 and Supplementary Tables S2, 3. The Z[Fe-(μ-O)-Zn] model fits the original EXAFS data of Fe and Zn species well, as shown in Fig. 1e, f and Supplementary Tables S2, 3, ensuring that the fitting results are reliable and enable an accurate demonstration of the local structure of isolated Fe and Zn atoms in the Fe_1-Zn_1/ZSM-5. The detailed fitting data show that the Fe atom is coordinated with one bridge oxygen (O_{BG}) and two framework oxygens (O_{FM}), respectively. In detail, for Fe species, the bond length of the Fe atom and the bridge oxygen (Fe-O_{BG}) is 2.0 Å, and the average bond length of the Fe atom and the framework oxygen (Fe-O_{FM}) is 2.1 Å. Furthermore, the fitting data of Fe species on the second shell indicates that the distance between Fe and Zn atoms is 2.7 Å, which is in line with the original EXAFS data (Fig. 1a, b) and the Fe-Zn path in Z[Fe-(μ-O)-Zn] model (Supplementary Fig. S12). For Zn species, Zn atoms are coordinated to one O_{BG} and two framework oxygens (O_{FM}), respectively. The bond length of the Zn atom to the bridge oxygen (Zn-O_{BG}) is 2.1 Å, and the average bond length of the Zn atom to the framework oxygen (Zn-O_{FM}) is 2.2 Å. Furthermore, the

https://doi.org/10.1038/s41467-025-64505-9

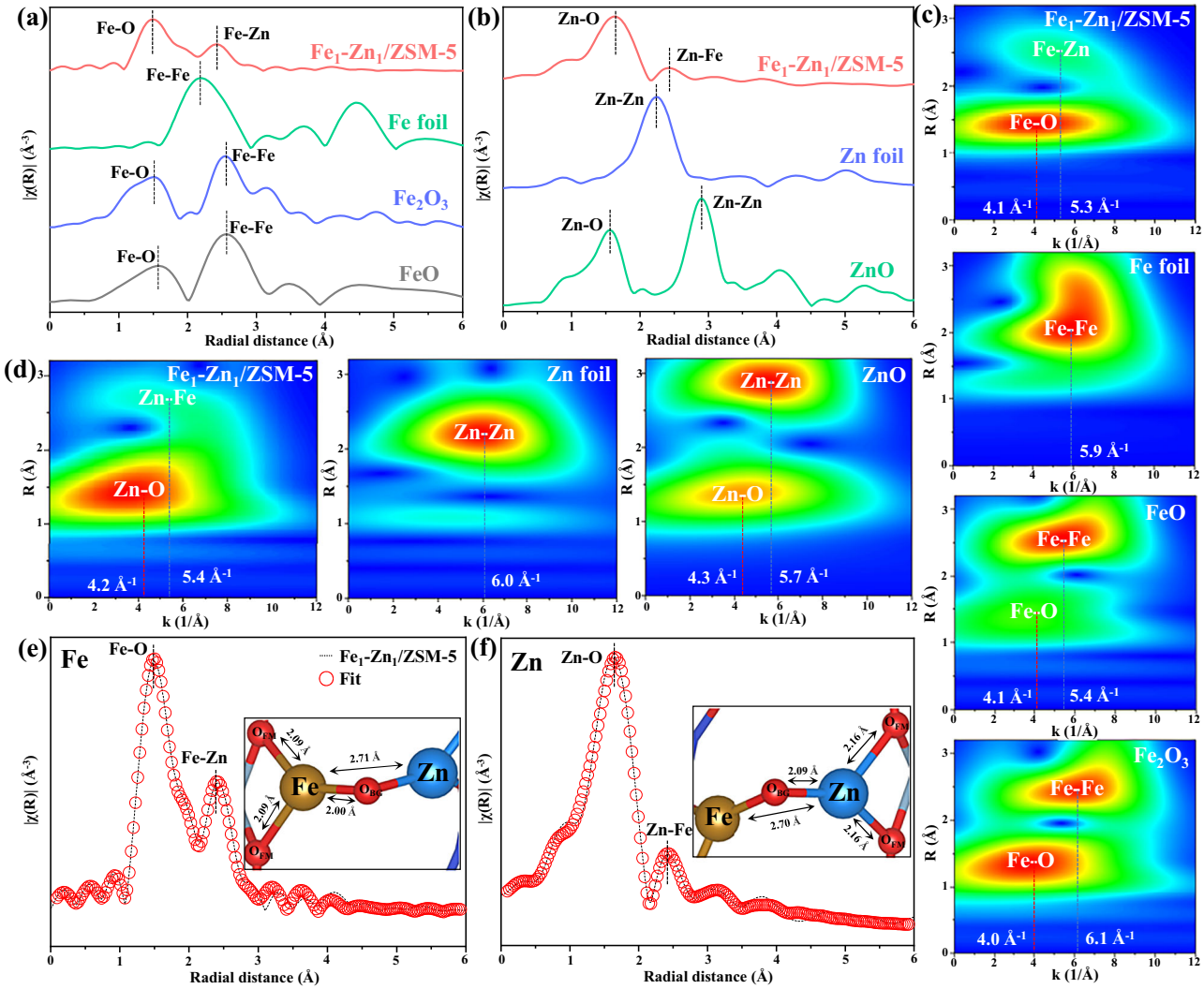

Fig. 1 | Construction and identification of Fe-(μ-O)-Zn dual-atom sites in Fe_1-Zn_1/ZSM-5 catalyst. a k^2-weighted μ(k) function of extended X-ray absorption fine structure (EXAFS) spectra of Fe spices. **b** EXAFS spectra of Zn spices. **c** Wavelet transform of the Fe K-edge EXAFS oscillations. **d** Wavelet transform of the Zn K-edge EXAFS oscillations; EXAFS fitting curve of (**e**) Fe and (**f**) Zn species in Fe_1-Zn_1/ZSM-5, the corresponding EXAFS K-space range used for the fitting is 2–12 $Å^{-1}$; Inset, proposed coordination environment of Fe-(μ-O)-Zn entity.

fitting data of Zn species on the second shell indicates that the distance between Fe and Zn atoms is 2.7 Å, which is in line with the fitting data for Fe species (2.7 Å) and the Zn-Fe path in Z[Fe-(μ-O)-Zn] model (Supplementary Fig. S12). The results further ensure the reliability of the geometric configurations of the Z[Fe-(μ-O)-Zn] site.

In addition, for Fe_1-Zn_1/ZSM-5 sample, five extra possible models (Z[Fe-(μ-O)$_2$-Zn], Z[Fe_1-Zn_2], Z[Fe-Zn], Z[Fe_2-Zn_3], and Z[Fe_2-Zn_1]) built for DFT calculation have been compared to fit the structure of active sites, but the significant deviation between the fitting curve and the original data excludes the possibility of Fe and Zn atoms existing as Z[Fe-(μ-O)$_2$-Zn] and Z[Fe-Zn], and also exclude the possibility of the small metal cluster species e.g., Z[Fe_1-Zn_2], Z[Fe_2-Zn_3], and Z[Fe_2-Zn_1]. Those results further verify the accuracy of the fitted Z[Fe-(μ-O)-Zn] structure in Fe_1-Zn_1/ZSM-5 (Supplementary Figs. S9–11, and Supplementary Tables S2, 3).

Fe-(μ-O)-Zn dual-atom sites mutually modulating the electronic states of Fe and Zn species

The electronic states of Fe and Zn species in Fe_1-Zn_1/ZSM-5 are further investigated by X-ray absorption near-edge structure (XANES). For Fe species, the absorption edge of Fe_1-Zn_1/ZSM-5 is higher than that of FeO but lower than that of Fe_2O_3 (Fig. 2a), indicating that the valence state of the Fe species is between Fe^{2+} and Fe^{3+} [24,35]. For Zn species, the absorption edge of Fe_1-Zn_1/ZSM-5 is higher than that of Zn foil but lower than that of ZnO (Fig. 2b), s state of the Zn atoms is between Zn^0 and Zn^{2+} [34]. The edge energy of the XANES further validates the above conclusion (Supplementary Fig. S13 and Supplementary Table S4). Furthermore, for the Zn species in Zn_1/ZSM-5, the electron paramagnetic resonance (EPR) spectrum has a signal at $g = 1.998$, which is associated with the Zn^+ species[36]. However, such a characteristic Zn^+ peak cannot be observed for the Fe_1-Zn_1/ZSM-5 (Supplementary Fig. S14), which reveals that the presence of Fe atoms regulates the electronic state of Zn species.

Furthermore, the X-ray photoelectron spectroscopy (XPS) was used to probe the electronic state of Fe and Zn species (Fig. 2c, d). For Fe_1/ZSM-5, there is one peak centered at 710.2 eV in the Fe $2p_{3/2}$, which can be assigned to the Fe^{3+}[37,38]. For the Fe_1-Zn_1/ZSM-5 sample, there is one peak centered at 709.8 eV in Fe $2p_{3/2}$, slightly shifting to a lower energy (0.4 eV) compared to that in Fe_1/ZSM-5, which is correspondingly assigned to the $Fe^{\delta+}$ ($2<\delta<3$) (Fig. 2c)[39]. For Zn_1/ZSM-5, the sole peak centered at 1021.8 eV in Zn $2p_{3/2}$ can be assigned to the Zn^+ species[40,41], which is in line with the EPR result (Supplementary Fig. S14). However, for Fe_1-Zn_1/ZSM-5 sample, the sole peak centered at 1022.0 eV in Zn $2p_{3/2}$ is slightly shifted to a higher energy compared to

https://doi.org/10.1038/s41467-025-64505-9

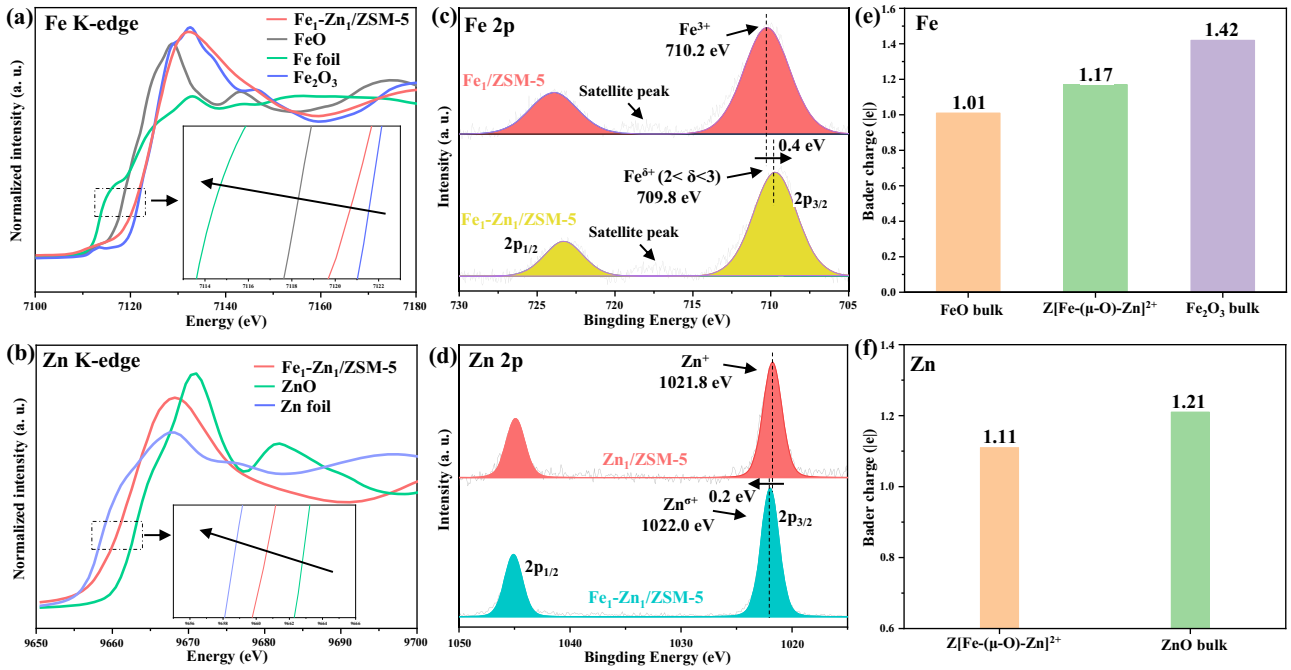

Fig. 2 | Electronic structure and chemical state of Fe-(μ-O)-Zn dual-atom sites in Fe_1-Zn_1/ZSM-5. a Fe K-edge X-ray absorption near-edge structure (XANES) spectra. Inset, pre-edge of the K-edge region of XANES. **b** Zn K-edge XANES spectra. Inset, pre-edge of the K-edge region of XANES. **c** XPS of Fe 2p for Fe_1-Zn_1/ZSM-5 and Fe_1/ZSM-5. **d** XPS of Zn 2p for Fe_1-Zn_1/ZSM-5 and Zn_1/ZSM-5. **e** Bader charge analysis of Fe in FeO bulk, $Z[Fe-(\mu-O)-Zn]^{2+}$, and Fe_2O_3 bulk. **f** Bader charge analysis of Zn in $Z[Fe-(\mu-O)-Zn]^{2+}$ and ZnO bulk.

that in Zn_1/ZSM-5 (1021.8 eV) but slightly lower than the Zn^{2+} (1022.2 eV), which suggests that the Zn species possesses the unique oxidation state of $Zn^{\sigma+}$ ($1 < \sigma < 2$)[41,42] (Fig. 2d). These results further imply that the electronic states of Fe and Zn have been mutually modulated in the Fe-(μ-O)-Zn dual-atom sites, which is in line with the XANES and EPR results.

To further understand the electronic state of Fe and Zn species in the as-synthesized samples, the experiments of diffuse reflectance infrared Fourier transform spectroscopy using NO as a probe molecule (NO-DRIFTs) were performed on the Fe_1/ZSM-5, Zn_1/ZSM-5, and Fe_1-Zn_1/ZSM-5 samples (Supplementary Fig. S15)[14,43,44]. Before each measurement, all the samples are preheated at 423 K for 2 h to remove the possible surface residual adsorbates. Due to the weak chemical interaction between Zn and NO species, no peaks associated with Zn-NO can be observed, which is in line with the open literature[45]. But for Fe species, there is only one peak centered at 1723 cm^{-1} in Fe_1/ZSM-5, which is associated with the NO linear adsorption on the Fe^{3+} sites (Fe^{3+}-NO)[46,47]. For the Fe_1-Zn_1/ZSM-5, the NO linear adsorption on Fe species red-shifting to 1715 cm^{-1} ($Fe^{\delta+}$-NO) compared with that on the Fe_1/ZSM-5, indicates that the oxidation state of Fe is slightly decreased[48], which confirms that the Zn atoms regulate the electronic state of Fe species. Additionally, the electron paramagnetic resonance (EPR) of the Fe center (Supplementary Fig. S16) further indicates the electronic states of Fe have been significantly modulated in the Fe-(μ-O)-Zn dual-atom sites, which is in line with the XANES, XPS, and NO-DRIFTs results. The UV-Vis diffuse reflectance spectra of Fe_1/ZSM-5, Zn_1/ZSM-5, and Fe_1-Zn_1/ZSM-5 (Supplementary Fig. S17) also verify the strong electronic interaction between neighboring Fe and Zn atoms[49,50].

To further explore the unique electronic states of Fe and Zn in Fe_1-Zn_1/ZSM-5, the Bader charge analysis and charge density difference calculations were performed using DFT. In Fig. 2e, the Bader charge of Fe in $Z[Fe-(\mu-O)-Zn]^{2+}$ (1.17 |e|) is higher than that of Fe in FeO bulk (1.01 |e|) but lower than that in Fe_2O_3 bulk (1.42 |e|). This confirms that the Fe species in Fe_1-Zn_1/ZSM-5 exhibit the unique electronic state of $Fe^{\delta+}$ ($2 < \delta < 3$), corroborating the XANES, XPS, and NO-DRIFTs data. For Zn species, the Bader charge of Zn in $Z[Fe-(\mu-O)-Zn]^{2+}$ (1.11 |e|) is slightly lower than that in ZnO (1.21 |e|) (Fig. 2f), verifying that the Zn species in Fe_1-Zn_1/ZSM-5 exhibit the unique electronic state of $Zn^{\sigma+}$ ($1 < \sigma < 2$). Furthermore, the Bader charges of Fe_1/ZSM-5 and Zn_1/ZSM-5 were calculated as shown in Supplementary Fig. S18. The Bader charge of Fe in $Z[Fe-(\mu-O)-Zn]^{2+}$ (1.17 |e|) is lower than that of Fe in $Z[Fe-(OH)_2]^+$ (1.39 |e|), which suggests that the Fe in $Z[Fe-(\mu-O)-Zn]^{2+}$ gains electrons compared to the Fe in $Z[Fe-(OH)_2]^+$. The Bader charge of Zn in $Z[Fe-(\mu-O)-Zn]^{2+}$ (1.11 |e|) is higher than that of Zn in Z[Zn] (0.72 |e|), which indicates that the Zn in $Z[Fe-(\mu-O)-Zn]^{2+}$ loses electrons compared with the Zn in $Z[Zn]^+$. Therefore, the electronic states of Fe and Zn are mutually modulated. The charge density difference plot of Fe_1-Zn_1/ZSM-5 further confirms the above conclusion, as shown in Supplementary Fig. S19. Moreover, the p-DOS analysis results (Supplementary Fig. S20) show that the Fe 3*d* orbital in Fe_1-Zn_1/ZSM-5 exhibits a *d*-band center position (upshift 2.15 eV) closer to the Fermi energy (E_f) compared with Fe_1/ZSM-5. These results further reveal that the introduction of Zn atoms regulates the electronic state of Fe species, which is in good agreement with the XANES, EPR, XPS, and NO-DRIFTs results. As the *d*-band center of Fe 3*d* shifts closer to the E_f in Fe_1-Zn_1/ZSM-5, it significantly promotes the directional and stable adsorption of O_2 on the Fe atom with a unilateral adsorption configuration ($Z[O_2$-Fe-(μ-O)-$Zn]^{2+}$), which correspondingly enhances the O_2 activation to form active Fe=O species under light irradiation. The active Fe=O oxygen species play the determining role in activating the C-H bond of CH_4, which will be thoroughly discussed later.

Fe-(μ-O)-Zn dual-atom sites achieving DOM to acetic acid under ambient temperature and pressure

To explore the catalytic performance of Fe_1-Zn_1/ZSM-5, DOM is performed in a photoreactor under the reaction condition of 50 mL/min CH_4 and 25 mL/min O_2 for 1 h, and H_2O as the reaction medium (details shown in Experimental Section in the Supplementary Information), which is out of the explosive limits of the CH_4/O_2 mixture system. The detections of gas mixture and liquid products are shown in

https://doi.org/10.1038/s41467-025-64505-9

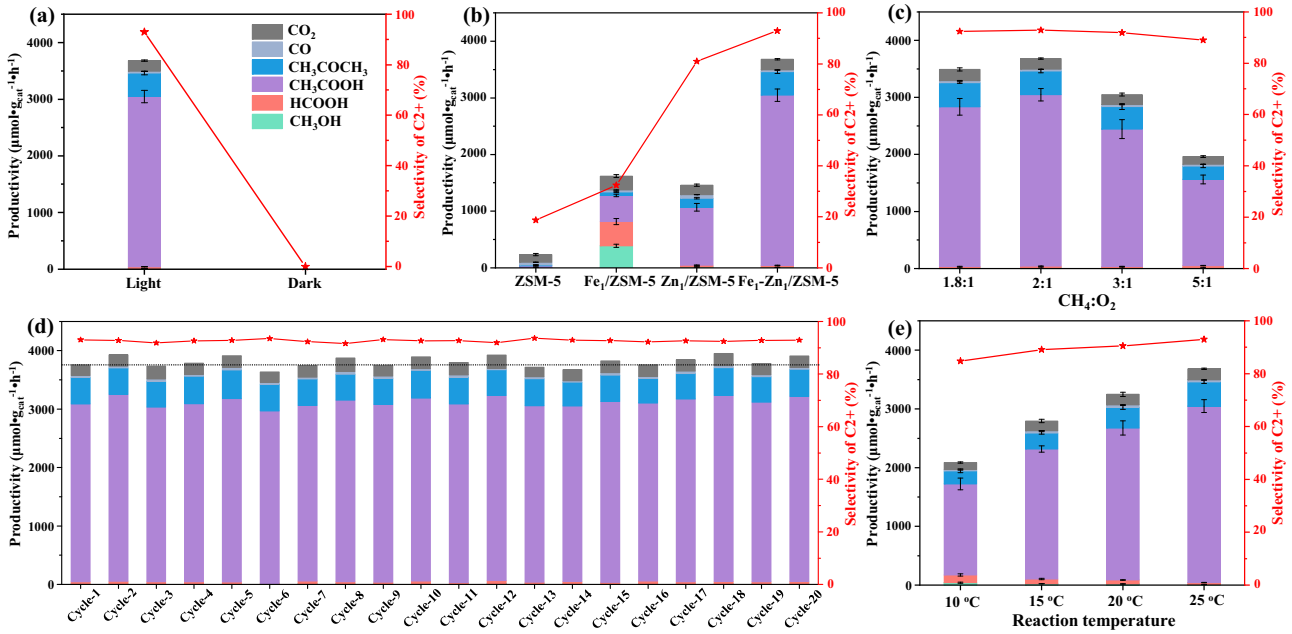

Fig. 3 | Catalytic performances for direct oxidation of methane. a Comparative experiments for DOM on Fe_1-Zn_1/ZSM-5 under light or dark conditions. **b** Yields and selectivity of C2+ on H-ZSM-5, Fe_1/ZSM-5, Zn_1/ZSM-5 and Fe_1-Zn_1/ZSM-5. **c** Yields and selectivity of C2+ of Fe_1-Zn_1/ZSM-5 on different flow rate ratios of CH_4 to O_2. **d** Reaction cycles of DOM over Fe_1-Zn_1/ZSM-5. **e** Yields and selectivity of C2+ of Fe_1-Zn_1/ZSM-5 on different temperatures. Reaction Condition (**a**): 20 mg catalysts dispersed in 100 mL deionized water, 50 mL/min CH_4 and 25 mL/min O_2 for 1 h at 25 °C; Reaction Condition (**b**) and (**d**): 20 mg catalysts dispersed in 100 mL deionized water, Hg lamp, 50 mL/min CH_4 and 25 mL/min O_2 for 1 h at 25 °C; Reaction Condition (**c**): 20 mg catalysts dispersed in 100 mL deionized water, Hg lamp for 1 h at 25 °C; Reaction Condition (**e**): 20 mg catalysts dispersed in 100 mL deionized water, Hg lamp, 50 mL/min CH_4 and 25 mL/min O_2 for 1 h. In (**a**–**c**) and (**e**), all data points were tested for three times to obtain the error bar.

Supplementary Figs. S21–23. As shown in Fig. 3a, no products can be observed after DOM over Fe_1-Zn_1/ZSM-5 under dark conditions, indicating that the DOM is driven by light irradiation. When introducing the light irradiation with a high-pressure mercury lamp (~220 to 1100 nm, the effective light intensity is 18.1 mW/cm^2 in the wavelength range of 220 and 240 nm) into the reaction over Fe_1-Zn_1/ZSM-5 for DOM, the yield of C2+ oxygenates is 3420 ± 137 μmol•g_{cat}^{-1}•h^{-1} with a selectivity of 93.0% in all products and the yield of acetic acid is 3006 ± 109 μmol•g_{cat}^{-1}•h^{-1} with a selectivity of 86.8% in all liquid products at 25 °C. The average CH_4 conversion rate over Fe_1-Zn_1/ZSM-5 is 0.13 ± 0.01%. The mass balance of carbon between the converted CH_4 and formed carbonaceous products is 98.4%, which secures that the measured data is reliable (Supplementary Fig. S24). Furthermore, when changing the methane or oxygen concentration, the Fe_1-Zn_1/ZSM-5 still shows excellent yield and selectivity of C2 + oxygenates, as shown in Supplementary Fig. S25 and Supplementary Fig. S26. Considering the heating effect of light irradiation, the ice and water mixture was used to sustain the set reaction temperature. Those results further indicate that the light irradiation plays a crucial role in the DOM in our reaction system. For DOM over pure H-ZSM-5 under the same reaction condition with light irradiation, the major product is CO_2 (57.7%) and the C2 + oxygenates productivity is only 44 ± 6 μmol•g_{cat}^{-1}•h^{-1}, around 78 times lower than that of Fe_1-Zn_1/ZSM-5, which indicates that the Fe-(μ-O)-Zn dual-atom sites are the main active sites (Fig. 3b). For DOM over Fe_1/ZSM-5, the yield of C1 oxygenates is 816 ± 82 μmol•g_{cat}^{-1}•h^{-1} (selectivity of 56.6%) and the yield of C2 + oxygenates is 524 ± 33 μmol•g_{cat}^{-1}•h^{-1} (selectivity of 32.4%), which indicates that the Zn sites play the crucial role in determining the coupling conversion of DOM. For DOM over Zn_1/ZSM-5, the major products are C2 + oxygenates (C2 + selectivity of 81.1%), and the yield is 1182 ± 83 μmol•g_{cat}^{-1}•h^{-1}, around 3 times lower than that of Fe_1-Zn_1/ZSM-5, which indicates that the Fe sites play the crucial role in boosting the catalytic activity for DOM. Meanwhile, the detailed control experiments by measuring the catalytic activity with similar loading content of metal sites over Fe_1/ZSM-5, Zn_1/ZSM-5, and Fe_1-Zn_1/ZSM-5 (the actual metal loadings measured by ICP-OES as shown in Supplementary Table S5) were conducted to exclude the influence of the density of metal sites (Supplementary Fig. S27). In addition, the yield of C2+ oxygenates for the physical mixtures of Fe_1/ZSM-5 and Zn_1/ZSM-5 with similar metal loading as that of Fe_1-Zn_1/ZSM-5 is only 1265 ± 94 μmol•g_{cat}^{-1}•h^{-1} with a selectivity of 59.8% in all products, around 2.7 times lower than that of Fe_1-Zn_1/ZSM-5, which clearly confirms the synergistic effects between Fe-(μ-O)-Zn dual-atom sites in Fe_1-Zn_1/ZSM-5 (Supplementary Fig. S28). By tuning the molar ratio of Fe/Zn, the yield of Fe_1-Zn_1/ZSM-5 with different Fe/Zn ratios for C2+ oxygenates is much higher than that of the sole Fe/ZSM-5 or sole Zn/ZSM-5, as shown in Supplementary Fig. S29. Moreover, by altering the loading content of Fe or Zn, the catalytic performance of Fe_1-Zn_1/ZSM-5 with similar Fe/Zn content (0.32 wt.% for Fe and 0.34 wt.% for Zn) for C2+ oxygenates is much better than that of the more or less Fe and Zn content, as shown in Supplementary Fig. S30. Moreover, the NO-DRIFTs results also reveal that altering the Fe/Zn ratio can notably regulate the oxidation state of Fe, and the excessive Fe atoms mainly exist in an isolated status similar to that of Fe_1-ZSM-5, which essentially exhibits higher oxidation states and benefits the formation of C1 oxygenates (Supplementary Fig. S31). Those results clearly indicate that the Fe-(μ-O)-Zn dual-atom sites in Fe_1-Zn_1/ZSM-5 not only promote the selectivity of C2+ oxygenates but also boost the catalytic activity for DOM.

To further identify the catalytic role of Fe-(μ-O)-Zn dual-atom sites in DOM, several control experiments have been performed. The catalytic yield of DOM over Fe_1-Zn_1/ZSM-5 is first investigated under the reaction atmosphere of different CH_4 and O_2 flow rates (Fig. 3c). An optimal flow ratio of CH_4 to O_2 is reached at 2:1. Over high or low ratio will decrease the productivity and selectivity of C2 + oxygenates, which indicates that the synergistic activation of CH_4 and O_2 plays a crucial role in the formation of C2+ oxygenates. In the absence of O_2, no products can be observed, which suggests that O_2 is the oxidant rather

than the H_2O (reaction medium) for DOM. In addition, the isotopic experiments ($^{18}O_2$) exhibit that the significant oxygenated products containing ^{18}O, e.g., $CH_3C^{18}O^{18}OH$, can be detected after the DOM when using $^{18}O_2$ as the oxidant (Supplementary Fig. S32). Moreover, the significant oxygenated products containing ^{16}O, e.g., $CH_3C^{16}O^{16}OH$, can be detected after the DOM when using $H_2{}^{18}O$ as the solvent (Supplementary Fig. S32). These isotopic experiment results indicate that it is the O_2 rather than the H_2O as the oxygen source to drive DOM in our catalyst system. In particular, DFT calculations also indicate that water did not serve as a cocatalyst or the oxidizing agents to assist methane activation (Supplementary Fig. S33). In the absence of CH_4, no products can be observed, which indicates that the carbon source is from the methane (Supplementary Fig. S34). Furthermore, the reaction order with respect to CH_4 (0.47) is higher than that of O_2 (0.16) as shown in Supplementary Fig. S35, indicating that the CH_4 activation for DOM on Fe_1-Zn_1/ZSM-5 is critical to the reaction kinetics[51], which is in line with the DFT simulation and will be discussed later.

To explore the stability of DOM over Fe_1-Zn_1/ZSM-5, we first probed the recycling stability. The obtained results reveal that there is no significant loss in the catalytic yield, methane conversion rate, and selectivity of C2+ oxygenates for at least 20 h (one hour for each reaction cycle, Fig. 3d and Supplementary Fig. S36). Then the stability was further analyzed by prolonging the reaction time. The total productivity of C2+ oxygenates is increased to 9744 ± 482 μmol•g_{cat}^{-1} after 4 h and 23,211 μmol•g_{cat}^{-1} after 24 h, as shown in Supplementary Fig. S37. Those results indicate that the Fe_1-Zn_1/ZSM-5 is stable during the DOM and enables to inhibition of the overoxidation of the formed C2+ oxygenates in the reaction atmosphere. The conditions used to regenerate the spent catalyst in each recycling measurement are listed in the Experimental Section. The SEM back-scatter images, XRD, and ICP-OES data of the used Fe_1-Zn_1/ZSM-5 sample after 20 cycles verify the leaching resistance ability of the Fe_1-Zn_1/ZSM-5 catalyst (Supplementary Figs. S38, 39 and SupplementaryTable S6).

The apparent activation energy (E_a) of the synthesized Fe_1-Zn_1/ZSM-5 catalysts was investigated to better understand the catalytic behavior of Fe_1-Zn_1/ZSM-5 (Supplementary Fig. S40). A similar method has been reported in previous literature[52]. The Fe_1-Zn_1/ZSM-5 exhibits the lowest E_a (25.7 kJ/mol) compared with that of Fe_1/ZSM-5 (34.1 kJ/mol) and Zn_1/ZSM-5 (30.4 kJ/mol), which indicates that the catalytic process of DOM is intrinsically boosted by Fe-(μ-O)-Zn dual-atom sites in Fe_1-Zn_1/ZSM-5 compared with the sole Fe or Zn single atoms. Moreover, the selectivity of C2+ oxygenates at 20 °C is 90.5%, which is close to that at 25 °C, although the productivity of C2+ oxygenates is only 2939 ± 153 μmol•g_{cat}^{-1}•h^{-1} (Fig. 3e). When further decreasing the reaction temperatures, the productivity of C2+ oxygenates is 2486 ± 77 μmol•g_{cat}^{-1}•h^{-1} with a selectivity of 89.1% at 15 °C and 1771 ± 130 μmol•g_{cat}^{-1}•h^{-1} with a selectivity of 84.8% at 10 °C, which suggests that the Fe-(μ-O)-Zn dual-atom sites possess excellent catalytic capability for DOM even below room temperature.

CH_4 activation promoted by active Fe = O oxygen species formed via O_2 photodissociation on Fe-(μ-O)-Zn dual-atom sites

To gain insights into the nature of the efficient promotion on CH_4 activation over Fe_1-Zn_1/ZSM-5 catalyst, density functional theory (DFT) calculations were further performed (Fig. 4a). The high-spin state was utilized for the Fe-Zn dual-atom site to perform the DFT calculation (Supplementary Table S7). We constructed the catalyst model according to the characterization results discussed in Section *2.1*. On the basis of the HAADF-STEM, EXAFS, and WT data of Fe_1-Zn_1/ZSM-5, the active site is a hetero-binuclear structure. Based on the above characterization data, several model active sites have been searched (Supplementary Figs. S9 and S10) but only the Z[Fe-(μ-O)-Zn]$^{2+}$ is the most reliable reaction site, where the distance of neighboring dual Fe and Zn atoms is 2.7 Å and the three-coordinated Fe and Zn atom located at the γ-8MR of ZSM-5 zeolite is connected by one bridged oxygen. Each dual-atom pair with three-fold coordination is connected by one bridged oxygen with neighboring Fe and Zn atoms. The detailed bond length and coordination structure of Fe/Zn species in the model active site fit the original EXAFS data well, which confirms the reliability of the model used in DFT calculations (Fig. 1e, f, Supplementary Table S2, and S3). Moreover, the previous calculation suggested that the framework Al^{3+} replacing the original Si^{4+} at T12 and T7 sites in the sinusoidal channel γ-8MR of ZSM-5 zeolite is the most energetically stable one to anchor Fe-(μ-O)-Zn atoms[13], which was further proved by pyridine-IR data (Supplementary Fig. S41 and Supplementary Table S8). In short, these results verify the reliability of the simulated Fe-(μ-O)-Zn dual-atom sites. The specific geometry structure of Z[Fe-(μ-O)-Zn]$^{2+}$ is listed in Supplementary Fig. S42.

Our DFT simulation results indicate that the bridging oxygen (μ-O) between Fe and Zn at the initial Z[Fe-(μ-O)-Zn]$^{2+}$ site is a divalent oxygen anion (Supplementary Fig. S9), which is difficult to directly abstract a hydrogen atom and activate the C-H bond of methane (barrier of 1.06 eV). Therefore, the cleavage of O_2 molecules by UV irradiation to generate the O* species adsorbed at the Z[Fe-(μ-O)-Zn]$^{2+}$ site is the first step to produce reactive oxygen species for DOM. Our comparative experiments with different photo energies confirm that the O_2 molecule was dissociated via a photochemistry rather than a photo-catalysis process in our reaction system (Supplementary Fig. S43). At first, O_2 is readily chemisorbed at the Fe site of Z[Fe-(μ-O)-Zn]$^{2+}$, which is exothermic by 1.50 eV. With the assistance of the photo, the O-O bond could be broken to simultaneously form Fe=O and another bridging O, thereby transforming the sites to Z[O=Fe-(μ-O)$_2$-Zn]$^{2+}$ (Supplementary Fig. S44). Specifically, in the range of the Herzberg continuum (from 218 to 239 nm) that was provided by the high-pressure mercury lamp in our reaction system, the O_2 enables to assimilation of light energy and excites the ground state oxygen $O_2(^3\sum_g^-)$ to the excited states $A(^3\sum_u^+)$, $c(^1\sum_u^-)$, and $A'(^3\Delta_u)$[53] Subsequently, the above excited states facilitate the cleavage of the O=O bond to generate O atoms, i.e., $O(^3P_2) + O(^3P_2)$, mainly through spin-orbit and orbit-rotation interactions[54,55]. Notably, due to the higher oxophilicity of Fe^{2+} compared with Zn^{2+} species[56], the oxygen atoms prefer to directionally adsorb over the Fe^{2+} site rather than the Zn^{2+} site at Z[Fe-(μ-O)-Zn]$^{2+}$. Thus, one of the $O(^3P_2)$ atoms coordinates with Fe and Zn atoms to form the bridging oxygen (μ-O), while the other $O(^3P_2)$ atom is stably anchored on the Fe site to generate the active oxygen species (Fe = O) at Z[O = Fe-(μ-O)$_2$-Zn]$^{2+}$ site (Fig. 4a). To sum up, the catalytic activation of methane using O_2 as oxidant at Z[Fe-(μ-O)-Zn]$^{2+}$ begins with the formation of Fe=O active species by photo-dissociation of O_2, then followed by the Fe=O species activating methane via a radical-like mechanism[57–59] (barrier of only 0.40 eV), which will be discussed later. In addition, the initial structure of the transition state with an energy barrier of 0.40 eV corresponds to a methane molecule located at the intersection between the straight channel and the sinusoidal channel of ZSM-5 (Supplementary Fig. S45). And if the physical adsorption of methane is considered, the activation energy barrier would be 0.44 eV.

To experimentally identify the reactive oxygen species (Fe=O) formed by O_2, the in situ Raman and DRIFTs were performed (Fig. 4b, c). When the O_2 and light irradiation were both introduced, the peak at 775 cm^{-1} associated with the Fe=O species was observed in the Raman spectra[60], which is in line with DFT calculation (IM1). Furthermore, when $^{16}O_2$ was replaced by $^{18}O_2$, a redshift of the characteristic peak of Fe=O species could be observed (Supplementary Fig. S46), further indicating the generation of Fe=O species[61]. Moreover, when the O_2 and light irradiation were both introduced, the same Fe=O species was observed at 843 cm^{-1} in the IR spectrum[48,62,63], which is consistent with the Raman data and DFT calculation. However, when the reaction conditions were changed into Ar with light off, Ar with light on, or O_2 with light off, none of the corresponding signals were detected in the Raman and IR spectra (Fig. 4b, c), which indicates that the O_2 and light

https://doi.org/10.1038/s41467-025-64505-9

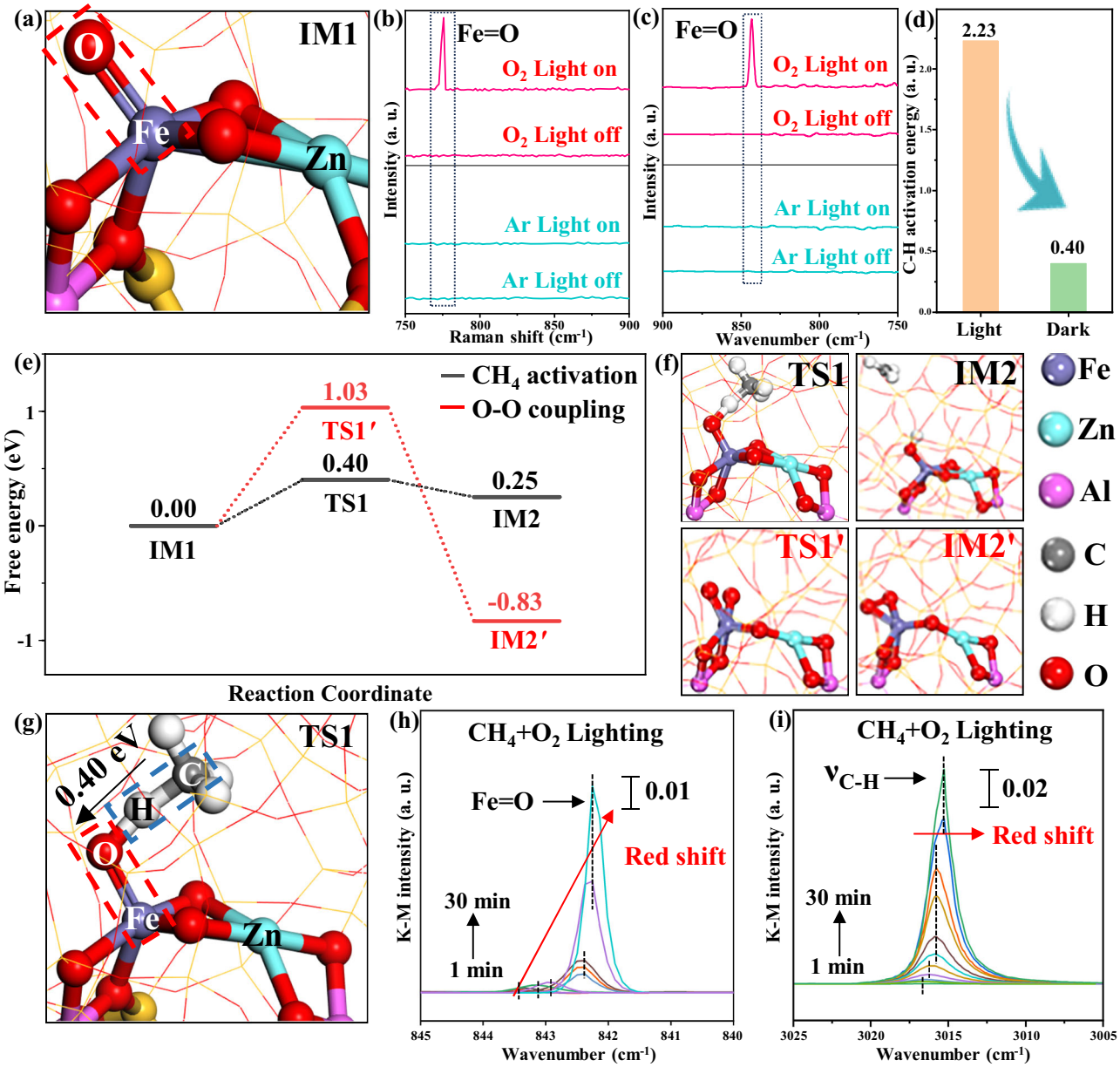

Fig. 4 | CH_4 activation enhanced by the Fe=O species on Fe-(μ-O)-Zn dual-atom sites. The unilateral state structure of Fe=O species at $Z[O=Fe-(\mu-O)_2-Zn]^{2+}$ site (**a**); The formation of Fe=O species captured by in situ Raman spectra under different conditions (**b**). The formation of Fe=O species captured by in situ FT-IR spectra under different conditions (**c**). The comparison on the CH_4 first C-H bond activation energy over Fe_1-Zn_1/ZSM-5 under light and dark conditions (**d**). The CH_4 activation and O-O coupling process at $Z[O=Fe-(\mu-O)_2-Zn]^{2+}$ site under irradiation (**e**). The geometry structures of transition states and intermediate species for CH_4 activation and O-O coupling process at $Z[O=Fe-(\mu-O)_2-Zn]^{2+}$ site (**f**). The transition state structure and the energy barrier to activate the first C-H bond of CH_4 for DOM over Fe_1-Zn_1/ZSM-5 (**g**). The process of Fe=O species activating CH_4 molecules captured by in situ DRIFTs (**h** and **i**). The Gibbs energy profile was calculated under the reaction conditions of 0.66 bar CH_4, 0.33 bar O_2 at 298 K. The H, C, O, Si, Al, Fe, and Zn atoms of the reaction sites are displayed in white, gray, red, yellow, pink, cerulean, and coral in the ball and stick style, respectively.

irradiation are necessary to generate active Fe=O species. In addition, our control experiments suggest that no products can be observed after the DOM in the absence of light irradiation or O_2 (Fig. 3a). These results provide solid evidence that the Fe=O species is the active oxygen species for CH_4 activation, which is consistent with the DFT simulation.

Importantly, the free energy barrier of activating the first C-H bond of CH_4 by the produced $Z[O=Fe-(\mu-O)_2-Zn]^{2+}$ sites with the assistance of light irradiation is only 0.40 eV, which is around 5 times lower than that on the $Z[O_2-Fe-(\mu-O)-Zn]^{2+}$ without light irradiation (2.23 eV, Fig. 4d). These results suggest that the Fe=O species, which are generated by Fe-(μ-O)-Zn dual-atom active sites with the assistance of O_2 photo-dissociation, can significantly boost the methane activation.

Moreover, the stability of Fe=O species is also investigated to probe the possibility of the Fe=O species transforming back into O_2 via the O-O coupling. By comparing the O-O coupling the free energy barrier of two O* and the free energy barrier of the first C-H bond cleavage in CH_4 (Fig. 4e, f), we can better understand the importance of $Z[O=Fe-(\mu-O)_2-Zn]^{2+}$ for CH_4 activation. For $Z[O=Fe-(\mu-O)_2-Zn]^{2+}$ (IM1), the O-O coupling free energy barrier (1.03 eV) of two O* is much higher than the free energy barrier of the first C-H bond cleavage in CH_4 (0.40 eV, TS1, Fig. 4g), so the Fe=O in $Z[O=Fe-(\mu-O)_2-Zn]^{2+}$ (IM1) would preferentially catalyze the CH_4 activation rather than the

recombination of two O* back into O_2. Conversely, for $Z[(O)_2\text{-}Fe\text{-}(OH)_2]^+$, the O-O coupling free energy barrier (0.19 eV) of two O* is lower than the first C-H bond cleavage in CH_4 (0.28 eV), indicating that two O* at $Z[(O)_2\text{-}Fe\text{-}(OH)_2]^+$ would be readily coupled to transform into $Z[(O_2)\text{-}Fe\text{-}(OH)_2]^+$ for mononuclear Fe_1/ZSM-5 (Supplementary Fig. S47). However, once $Z[(O_2)\text{-}Fe\text{-}(OH)_2]^+$ is formed, the free energy barrier of methane C-H bond activation surges to 1.36 eV, indicating that mononuclear Fe_1/ZSM-5 is deactivated. These results indicate that the mononuclear Fe_1/ZSM-5 is unable to effectively activate CH_4 compared with that of Fe_1-Zn_1/ZSM-5 binuclear sites. For the $Z[O=Fe\text{-}(\mu\text{-}O)_2\text{-}Fe]^{2+}$, the O-O coupling free energy barrier (2.74 eV) of two O* is also higher than the first C-H bond cleavage in CH_4 (0.96 eV), but its free energy barrier to cleave the first C-H bond in CH_4 is much higher than that of $Z[O=Fe\text{-}(\mu\text{-}O)_2\text{-}Zn]^{2+}$ (0.40 eV). Therefore, the catalytic capability of $Z[O=Fe\text{-}(\mu\text{-}O)_2\text{-}Fe]^{2+}$ to activate methane is lower than that of $Z[O=Fe\text{-}(\mu\text{-}O)_2\text{-}Zn]^{2+}$ (IM1). Consequently, comparing the C-H bond activation and O-O coupling over hetero-binuclear Fe_1-Zn_1/ZSM-5, homo-binuclear Fe_1-Fe_1/ZSM-5, and mononuclear Fe_1/ZSM-5 (Supplementary Fig. S48), we could find that the synergistic effects between Fe-(μ-O)-Zn dual-atom sites not only stabilize the reactive oxygen species, but also exhibit better capability for the activation of C-H bond in CH_4. Furthermore, we have computationally compared the first C-H bond activation of the CH_4 free energy barrier of hetero binuclear $Z[O=Fe(\mu\text{-}O)_2\text{-}Zn]^{2+}$, $Z[O=Fe(\mu\text{-}O)_2\text{-}Cu]^{2+}$, and $Z[O=Fe(\mu\text{-}O)_2\text{-}Ni]^{2+}$ (Supplementary Fig. S49a). The order of the free energy barriers for the C-H bond activation follows as $Z[O=Fe\text{-}(\mu\text{-}O)_2\text{-}Zn]^{2+}$ (0.40 eV) < $Z[O=Fe\text{-}(\mu\text{-}O)_2\text{-}Cu]^{2+}$ (0.51 eV) < $Z[O=Fe\text{-}(\mu\text{-}O)_2\text{-}Ni]^{2+}$ (0.54 eV), which indicates the Fe-(μ-O)-Zn dual-atom sites enhance performance, facilitate the C-H bond activation (Supplementary Fig. S49b). Meanwhile, for DOM over Fe_1-Ni_1/ZSM-5 and Fe_1-Cu_1/ZSM-5, the yield of C2+ oxygenates is 1993 ± 86 μmol•g_{cat}^{-1}•h^{-1} (C2+ oxygenates selectivity of 81.9%) on Fe_1-Ni_1/ZSM-5 and 2488 ± 150 μmol•g_{cat}^{-1}•h^{-1} (C2 + oxygenates selectivity of 92.3%) on Fe_1-Cu_1/ZSM-5, which are lower than the yield and selectivity of C2 + oxygenates on Fe_1-Zn_1/ZSM-5 (3420 ± 137 μmol•gcat^{-1}•h^{-1} with a selectivity of 93.0%). Those results verify that the synergistic effects of Fe-(μ-O)-Zn dual-atom sites enable to enhance the performance for DOM to C2+ oxygenates (Supplementary Fig. S49c).

The process of Fe=O species activating CH_4 molecules was further validated by the in situ DRIFTs. When both CH_4 and O_2 were introduced under light irradiation, the peak associated with the Fe=O stretch vibration is gradually redshifted as the reaction proceeds (Fig. 4h) and the C-H stretch vibration of CH_4 on Fe_1-Zn_1/ZSM-5 is also gradually redshifted (Fig. 4i), which confirms the methane activation is triggered by the Fe=O species for DOM on Fe_1-Zn_1/ZSM-5. Alternatively, only when sole O_2 or sole CH_4 was introduced under light irradiation, there is no shifting on Fe=O species and C-H stretch vibration of CH_4 (Supplementary Figs. S50, S51). Furthermore, the in situ O_2-DRIFTs under light irradiation and switch to CH_4-DRIFTs under dark indicate that Fe=O active species are formed by light-driven O=O bond dissociation, and the C-H activation in CH_4 is triggered by the formed Fe=O species (Supplementary Fig. S52). Those results confirm that the methane activation is triggered by the Fe=O species for DOM on Fe_1-Zn_1/ZSM-5, which is in line with the DFT calculation.

In addition, H_2O_2 is also observed in the liquid determined by the potassium titanium oxalate method[64] after DOM, and the concentration is 231 ± 9.2 μM, as shown in Supplementary Fig. S53. Some previous works reported that H_2O_2 or its derived •OH radicals are the reactive oxygen species for the DOM[65,66]. To identify whether H_2O_2 is the reactive oxygen species for the DOM in our reaction system, the DOM is conducted by externally adding H_2O_2 rather than O_2. Only a trace amount of methanol (14 μmol•g_{cat}^{-1}•h^{-1}) is observed in the liquid after DOM when the externally added H_2O_2 is used as an oxidant with a similar concentration (~ 231 μM, Supplementary Fig. S54). These results indicate that the H_2O_2 species that existed in the solution is not the reactive oxygen species for DOM on our catalyst system. In addition, to identify whether the hydroxyl radicals (•OH) formed by the dissociation of H_2O_2 are the active oxygen species for the DOM, Na_2S was added as a •OH scavenger[23] to conduct the comparison experiment for DOM. The comparison experiments exhibit a similar yield of the C2+ products ($3{,}413 \pm 179$ μmol•g_{cat}^{-1}•h^{-1}, Supplementary Fig. S55), which indicates that the •OH produced by H_2O_2 is not the reactive oxygen species for DOM as well. These results further confirm that only the Fe=O species in $Z[O=Fe\text{-}(\mu\text{-}O)_2\text{-}Zn]^{2+}$ (IM1) is the reactive oxygen species for DOM.

Fe-(μ-O)-Zn dual-atom sites boosting C-C coupling for DOM toward acetic acid via synergistic-tandem mechanism

To further clarify the reaction pathway of DOM over Fe_1-Zn_1/ZSM-5 catalyst, the reaction mechanism for the production of CH_3COOH, which is the main C2+ product on $Z[O = Fe\text{-}(\mu\text{-}O)_2\text{-}Zn]^{2+}$ site, was computationally investigated (Fig. 5a). The models for key intermediate species confined in the channels of the Fe_1-Zn_1/ZSM-5 by DFT calculation are also shown in Fig. 5a, b. After the first C-H bond in CH_4 is activated by Fe=O species through the radical-like mechanism (IM1 and IM2 shown in Fig. 4f), the generated methyl radicals can be readily captured by the bridge oxygen at $Z[(HO)\text{-}Fe\text{-}(\mu\text{-}O)_2\text{-}Zn]^{2+}$ (IM2 in Fig. 4f), which is energetically lowered by 2.33 eV. Then, the second C-H bond of CH_4 can be activated by the hydroxyl to generate $Z[(H_2O)(HCHO)\text{-}Fe\text{-}(\mu\text{-}O)\text{-}Zn]^{2+}$ (IM4 in Fig. 5b), which needs to overcome a free energy barrier of 0.67 eV (TS2). The water molecules at $Z[(H_2O)(HCHO)\text{-}Fe\text{-}(\mu\text{-}O)\text{-}Zn]^{2+}$ (IM4) are desorbed from Fe atoms to generate $Z[HCHO\text{-}Fe\text{-}(\mu\text{-}O)\text{-}Zn]^{2+}$ (IM5), and the desorption energy is 0.84 eV. In addition, there is a possible side reaction to generate HCOOH, which is carried out by dehydrogenation of formyl aldehyde (HCHO*) of IM5 to μ-O (Supplementary Fig. S56). But for $Z[HCHO\text{-}Fe\text{-}(\mu\text{-}O)\text{-}Zn]^{2+}$ (IM5), the branch to generate formic acid is energetically less favorable than the acetic acid branch, starting with the migration of HCHO* from the Fe site to the Zn site that only necessitates the energy input of 0.36 eV. It indicates that the acetic acid would be easier to produce than formic acid, which is consistent with our experimental results. Then, the chemisorbed formyl aldehyde (HCHO*) at the Fe site can easily migrate to the Zn site, with a free energy barrier of 0.36 eV (Supplementary Fig. S57), which is exothermic by 1.13 eV and correspondingly generates $Z[Fe\text{-}(\mu\text{-}O)\text{-}Zn\text{-}(HCHO)]^{2+}$ (IM6) site. Then, a second Fe=O species can be produced again by photo-assisted O_2 dissociation to generate $Z[O=Fe\text{-}(\mu\text{-}O)_2\text{-}Zn\text{-}(HCHO)]^{2+}$ (IM7) as discussed in *Section 2.4*. In addition, compared with the Fe-Fe diatomic site, the desorption free energy (0.83 eV) of the formyl aldehyde at the $Z[O=Fe\text{-}(\mu\text{-}O)_2\text{-}Zn\text{-}(HCHO)]^{2+}$ (IM7) site is higher than that at the $Z[O=Fe\text{-}(\mu\text{-}O)_2\text{-}Fe\text{-}(HCHO)]^{2+}$ site (0.43 eV) (Supplementary Fig. S58). This indicates that the Fe-(μ-O)-Zn dual-atom site can stabilize the intermediates generated by methane, thereby promoting the C-C coupling of the intermediates to generate C2 + products.

The second CH_4 could still be readily activated by Fe=O species at the $Z[O=Fe\text{-}(\mu\text{-}O)_2\text{-}Zn\text{-}(HCHO)]^{2+}$ (IM7) site through the radical-like mechanism to produce a methyl radical and $Z[OH\text{-}Fe\text{-}(\mu\text{-}O)_2\text{-}Zn\text{-}(HCHO)]^{2+}$ (IM8) site, which requires a free energy barrier of 0.46 eV (TS3). The efficient methane activation by alpha oxygen of Fe=O through the radical-like mechanism enables the barrierless C-C bond coupling between the formed methyl radical and HCHO* to generate $Z[(OH)(O)\text{-}Fe(\mu\text{-}O)\text{-}Zn\text{-}(CH_3CH_2O)]^{2+}$ (IM9), which is exothermic by 0.60 eV. Thus, the alpha hydrogen of open-shell CH_3CH_2O* at $Z[(OH)(O)\text{-}Fe(\mu\text{-}O)\text{-}Zn\text{-}(CH_3CH_2O)]^{2+}$ (IM9) site could be readily abstracted by the oxygen adsorbed at Fe site, and then the $Z[(OH)\text{-}Fe(\mu\text{-}O)(\mu\text{-}OH)\text{-}Zn\text{-}(CH_3CHO)]^{2+}$ (IM10) site is generated, which only needs to overcome a free energy barrier of 0.17 eV (TS4). The process of IM10 → IM11 ($Z[(OH)\text{-}Fe(\mu\text{-}O)(\mu\text{-}OH)\text{-}Zn\text{-}(CH_3CHO)]^{2+}$) involves two steps: C-H bond cleavage of CH_3CHO* and Zn-O bond cleavage for the switch of adsorption moiety of CH_3CO* from carbonyl O to C (Supplementary

https://doi.org/10.1038/s41467-025-64505-9

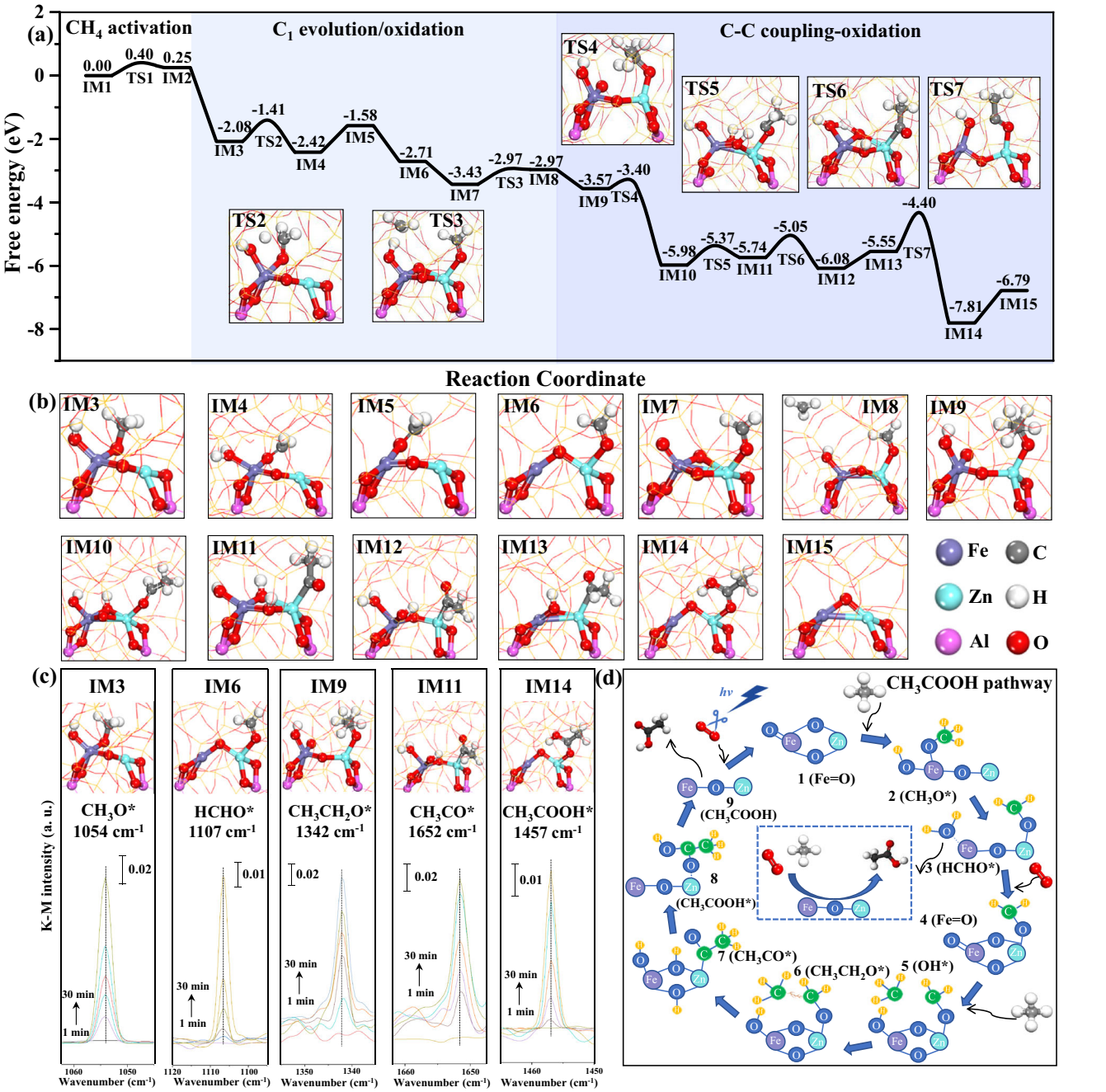

Fig. 5 | Reaction procedures of DOM toward acetic acid over Fe_1-Zn_1/ZSM-5. Reaction pathways for DOM to CH_3COOH over Fe_1-Zn_1/ZSM-5 (**a**). The geometric structures of the key transition states for CH_3COOH formation and oxidative dehydrogenation (**b**). The experimentally captured intermediates by FT-IR spectra of $CH_4 + O_2$ under light irradiation over Fe_1-Zn_1/ZSM-5 (**c**). Schematic illustration of the Fe-(μ-O)-Zn active sites catalyzing DOM to CH_3COOH (**d**). The Gibbs energy profile was calculated under the reaction conditions of 0.66 bar CH_4, 0.33 bar O_2 at 298 K. The H, C, O, Si, Al, Fe, and Zn atoms of the reaction sites are displayed in white, gray, red, yellow, pink, cerulean, and coral in the ball and stick style, respectively.

Fig. S59). For IM10, CH_3CHO^* could be dehydrogenated by the μ-O to generate CH_3CO^* that is chemisorbed atop the Zn site through the carbonyl oxygen of CH_3CO^*, with a free energy barrier of 0.61 eV. Then, the adsorption moiety of CH_3CO^* would be readily transformed from carbonyl oxygen to carbonyl carbon, together with the Zn-O bond cleavage and C-Zn bond formation, which only needs to overcome a free energy barrier of 0.17 eV. Then the hydrogen atom transfer from the bridged hydroxyl to the non-bridge hydroxyl will generate $Z[(H_2O)\text{-Fe-}(\mu\text{-OH})(\mu\text{-O})\text{-Zn-}(CH_3CO)]^{2+}$ (IM12), which only requires a free energy barrier of 0.69 eV (TS6). Subsequently, the water molecule can desorb from the Fe atom to generate $Z[(OH)\text{-Fe-}(\mu\text{-O})\text{-Zn-}(CH_3CO)]^{2+}$ (IM13), and the desorption free energy is only 0.53 eV. IM13 → IM14 undergoes the transformation of the adsorption configuration of CH_3CHO^*, followed by the C-O coupling for acetic acid formation (Supplementary Fig. S60). The transformation of the adsorption configuration of CH_3CO^* from carbonyl carbon to carbonyl oxygen requires a free energy barrier of 0.51 eV. Then, CH_3CO^* can couple with OH* to generate CH_3COOH^* by overcoming a free energy barrier of 0.85 eV, which is significantly exothermic by 2.56 eV. Then, the CH_3COOH can desorb from the $Z[Fe\text{-}(\mu\text{-O})\text{-Zn-}(CH_3COOH)]^{2+}$ (IM14) site to regenerate the active site of $Z[Fe\text{-}(\mu\text{-O})\text{-Zn}]^{2+}$(IM15), requiring an energy input of 1.02 eV.

To experimentally verify the proposed reaction pathway, the in situ DRIFTs of $CH_4 + O_2$ on Fe_1-Zn_1/ZSM-5 under light irradiation were conducted. As shown in Fig. 5c, the peaks at 1054 cm^{-1} and 1107 cm^{-1} are associated with the stretching vibration of C-O in the adsorbed CH_3O^* (IM3) and HCHO* (IM6) species, respectively[67,68], which are in line with our DFT simulation. Meanwhile, the externally added formaldehyde was conducted to further verify the catalytic role of the HCHO* intermediate. The yield of acetic acid significantly increased with the enhancement of externally added formaldehyde (Supplementary Fig. S61 and S62). However, when CH_4 was removed and only HCHO and O_2 were added, no CH_3COOH was detected (Supplementary Fig. S61). These results suggest that HCHO* and intermediates formed by CH_4 play a pivotal role in the formation of acetic acid. Under dark conditions, no CH_3COOH was detected, which indicates that the formation of acetic acid is driven by light irradiation (Supplementary Fig. S63). The peak at 1342 cm^{-1} is associated with the bending vibrations of C-H in the adsorbed $CH_3CH_2O^*$ (IM9) species[69], which is the key intermediate to C2+ after the C-C coupling reaction on Fe-(μ-O)-Zn dual-atom sites. The peaks at 1652 cm^{-1} and 1457 cm^{-1} are ascribed to the stretching vibrations of C=O of the adsorbed CH_3CO^* (IM11) and CH_3COOH^* (IM14) species, respectively[70,71], which are the intermediates generated by the further oxidation of $CH_3CH_2O^*$ (IM9) after C-C coupling on Fe-(μ-O)-Zn dual-atom sites. Meanwhile, no signals can be observed from the in situ DRIFTs when there is no oxygen or light irradiation, which further indicates that the photo-assisted O_2 activation plays a crucial role in the DOM (Supplementary Fig. S64 and S65). The significant redshifts of C-O/C-H vibration frequency acquired by isotope-labeling $^{13}CH_4 + O_2$ DRIFTS further verify the accuracy of the assignment of the CH_3O^*, $HCHO^*$, and $CH_3CH_2O^*$ intermediates experimentally captured by FT-IR spectra of $^{12}CH_4 + O_2$ under light irradiation over Fe_1-Zn_1/ZSM-5 (Supplementary Fig. S66). These intermediates observed from in situ DRIFTs experimentally verify the reliability of the DFT calculation for the reaction pathway of DOM (Fig. 5a). The tandem catalysis process triggered by Fe=O species under light irradiation was further verified by the stepwise reaction process, as shown in Supplementary Fig. S67.

Hence, according to the above DFT calculation, in situ characterization results and formaldehyde-as-reactant control experiments, the most possible reaction pathway of DOM to acetic acid on Fe_1-Zn_1/ZSM-5 is proposed as steps 1-9 in Fig. 5d, and the comprehensive reaction cycles including 14 steps are listed in Supplementary Fig. S68.

$$O_2(g) \xrightarrow{h\nu} O^* + \mu(O) \quad (1)$$

$$CH_4(g) + O^* + \mu(O) \rightarrow CH_3O^* + OH^* \quad (2)$$

$$CH_3O^* + OH^* \rightarrow HCHO^* + H_2O \quad (3)$$

$$O_2(g) \xrightarrow{h\nu} O^* + \mu(O) \quad (4)$$

$$CH_4(g) + O^* \rightarrow \bullet CH_3 + OH^* \quad (5)$$

$$\bullet CH_3 + HCHO^* \rightarrow CH_3CH_2O^* \quad (6)$$

$$CH_3CH_2O^* + 2\mu(O) \rightarrow CH_3CO^* + 2\mu(OH) \quad (7)$$

$$CH_3CO^* + OH^* \rightarrow CH^3COOH^* \quad (8)$$

$$CH_3COOH^* \xrightarrow{Desorption} CH_3COOH(aq) \quad (9)$$

Those results indicate the Fe-(μ-O)-Zn dual-atom sites have significantly promoted DOM toward acetic acid via the synergistic-tandem mechanism.

Discussion

In summary, we designed and constructed the Fe-(μ-O)-Zn dual-atom sites by supporting Fe and Zn atoms on ZSM-5 (Fe_1-Zn_1/ZSM-5), which achieved the DOM by O_2 to acetic acid under ambient temperature and pressure. The Fe_1-Zn_1/ZSM-5 yields a C2+ productivity of 3420 ± 137 μmol•g_{cat}^{-1}•h^{-1} and a C2+ selectivity of 93.0% in all products (the selectivity of acetic acid is 86.8%) and sustains the original activity for at least 20 h (one hour for one reaction cycle) at 25 °C and ambient pressure under light irradiation. The comprehensive characterization results reveal that with the assistance of the ultraviolet light, the Fe-(μ-O)-Zn active sites boost the stable formation of highly reactive Fe=O species and provide dual reaction sites, which promote the activation of the C-H bond of CH_4 and the C-C coupling reaction. Although further refinement in optimizing the reaction conditions and other factors may improve the catalytic performance, this work should broaden the avenue towards the sustainable conversion of methane to value-added C2+ products under ambient temperature and pressure.

Methods

Synthesis of catalysts

The modified adsorption methods were used to prepare the H-ZSM-5 supported Fe and Zn dual atoms (Fe_1-Zn_1/ZSM-5) via finely tuning the adsorption parameters in the aqueous solution[13–18]. Typically, H-ZSM-5 (The Si/Al molar ratio of ZSM-5 is 12.5:1, the Brunauer-Emmett-Teller (BET) surface area of ca. 310 m^2/g; Tianjin Yuanli Chemical Co.) was dispersed in deionized water (18.2 MΩ cm^{-1}), and the pH of the H-ZSM-5 solution was finely tuned from 4.5 to 3.0 by using HCl aqueous. The Fe & Zn precursor solutions ($HFeCl_4$ is prepared by $FeCl_3$ and HCl[72]. Typically, dissolving 135.10 g of $FeCl_3 \cdot 6H_2O$ in a small amount of water, and prepare 542 mL of 12 mol/L HCl solution. Then, transferring both solutions to a 1 L volumetric flask and dilute to the mark with water to synthetize $HFeCl_4$. $FeCl_3$ and $ZnCl_2$ is purchased from Sinopharm Chemical Reagent Co., China), were simultaneously pumped into the H-ZSM-5 suspension with a speed of ~ 0.2 ml/min under stirring, and the solution underwent irradiation treatment with ultraviolet light (5 W LED, wavelength 254 nm) for 4 h at 5 ± 2 °C. After aging for 4 h at 5 ± 2 °C, the sample was centrifuged, washed, and then dried at 40 °C in a vacuum and calcined at 350 °C for 4 h in Ar flow. It has been reported that the introduction of UV light can promote the synthesis of heteronuclear dual-atom catalysts since the second metal atoms (M2) are prone to navigation and positioning to the first metal atoms (M1) after reacting with photogenerated electrons near the M1 site[19–21]. Similarly, under UV irradiation, the Fe^{3+} from $HFeCl_4$ and Zn^{2+} from $ZnCl_2$ form Fe_1-Zn_1 dual-atom sites. The actual loadings of Fe (0.324 wt.%) and Zn (0.344 wt.%) were measured by the inductively coupled plasma optical emission spectroscopy (ICP-OES) method. The other Fe_1-Ni_1/ZSM-5, Fe_1-Cu_1/ZSM-5, were prepared in a similar manner by using $NiCl_2 \cdot 6H_2O$, $CuCl_2 \cdot 2H_2O$, and $FeCl_3$ (Sinopharm Chemical Reagent Co., China) as metal precursors.

Evaluation of catalytic performance

DOM was performed in a 240 mL photoreactor equipped with a quartz window. The catalyst (typically 20 mg) was dispersed in 100 mL deionized water (18.2 MΩ cm^{-1}). The photoreactor was sealed and completely degassed through a vacuum pump to remove the possible

dissolved air in the deionized water. Then the mixture gas of methane (typically 50 ml/min) and oxygen (typically 25 ml/min) was introduced into the solution by inserting a gas pipeline below the liquid surface and stirred vigorously at ca. 1200 rpm. Subsequently, the reactor was irradiated by a 500 W high-pressure mercury lamp (~220 to 1100 nm, the effective light intensity is 18.1 mW/cm^2 in the wavelength range of 220 and 240 nm measured by OHSP-350UVS) for 1 h. During the reaction, the temperature of the liquid was maintained at the desired reaction temperature (typically 25 °C) by the ice and water mixture. The reactor was connected with gas chromatography (GC 2060, Shanghai Ruimin Instrument Co., Ltd), and then the gaseous composition was directly analyzed by GC (column type: TDX-01) equipped with a methanizer unit and FID detector. Only CO, CO_2, and CH_4 could be detected in a typical GC of a gas mixture after DOM (Supplementary Fig. S21). Oxygenates in the liquid were analyzed by ^{1}H NMR spectra on a Bruker 400 MHz NMR. Typically, 0.7 mL of product solution was mixed with 0.1 mL D_2O (with 0.1012 μmol DSS) in the tube to conduct NMR measurement. 3-(trimethylsilyl)-1-propanesulfonic acid sodium salt (DSS, purchased from TCI) was used as a calibration standard. The solvent suppression technique was run to suppress the dominant H_2O signal during NMR measurement. The experimental detailed for ^{1}H-NMR were as follows: a pulse sequence of noesygppr1d was used with a spectral width of 15 ppm, 64 k data points, an acquisition time of 8.19 seconds, 32 scans, a pre-scan delay of 6.50 μs, delays of 30 s, and a transmitter frequency offset of 4.699 ppm. The ^{1}H NMR spectra of liquid products over Fe_1-Zn_1/ZSM-5 after DOM are shown in Supplementary Fig. S22. The identified oxygenated products in liquid were acetic acid (δ = 2.07 ppm), acetone (δ = 2.22 ppm), methanol (δ = 3.34 ppm), and formic acid (δ = 8.28 ppm). To quantify the products accurately, their standard curves were established, respectively (Supplementary Fig. S23). Considering that CH_4 is a flammable gas, it should be mentioned that all the CH_4 concentrations (64.2 ~ 83.3 vol.%) we used in this work are out of the explosive limits of CH_4/O_2 mixtures (5.4 ~ 59.2 vol.%).

Theoretical calculation methods

To explore the mechanism of direct oxidation of methane to acetic acid over Fe_1-Zn_1/ZSM-5, periodic density functional theory (DFT) calculations were performed using the Vienna Ab-initio Simulation Package (VASP5.4.1)[73]. The projector augmented wave (PAW) method was used to describe the interaction between the atomic nucleus and electrons, with a cutoff energy for the plane wave set to 450 eV[74]. We used the generalized gradient approximation (GGA) Perdew-Burke-Ernzerhof (PBE) functional to describe the exchange-correlation interactions[75]. The Key van der Waals interactions in molecular sieves were accounted for using the DFT-D3 (BJ) method[76]. The convergence criterion for the maximum force on all relaxed atoms was set to 0.05 eV/Å. The transition states were located using the constraint minimization method with the same force convergence criterion[77]. We carefully compared all the possible spin configurations and utilized the most stable spin configuration in the manuscript. As shown in Supplementary Table S7, the ferromagnetic S = 2/2 state of high-spin and the S = 0 state of low-spin status could be finally located for [O=Fe-(μ-O)$_2$-Zn]$^{2+}$. Hence, the most stable ferromagnetic S = 2/2 state of high spin was used for Fe-Zn dual-atom sites. For Z[O = Fe-(μ-O)$_2$-Fe]$^{2+}$, four spin configurations were found, among which the ferromagnetic S = 6/2 of the high spin was the most stable one. The energy difference between S = 6/2 and metastable S = 4/2 is trivial. Therefore, the high-spin state as the method was utilized for Fe-Zn and Fe-Fe dual-atom site to perform the DFT calculation. Several groups have reported that the molecular entropy loss confined within the pores of ZSM-5 zeolite is 38% relative to the gas phase[78]. Therefore, the entropy of small molecules in ZSM-5 zeolite was corrected by this value. Details on the Gibbs free energy calculations, including zero-point energy, internal energy, and entropy contributions, can be found in our previous work and Supplementary Information[15,22].

Data availability

The data supporting the findings of this study are included within the article and its Supplementary Information files. The data generated in this study are provided in the Source Data file. Source data are provided in this paper. All data are available upon request from the corresponding authors.

References

1. Mao, J. et al. Direct conversion of methane with O_2 at room temperature over edge-rich MoS_2. *Nat. Catal.* **6**, 1052–1061 (2023).
2. Ding, J. et al. A tin-based tandem electrocatalyst for CO_2 reduction to ehanol with 80% selectivity. *Nat. Energy* **8**, 1386–1394 (2023).
3. Lin, M. & Sen, A. Direct catalytic conversion of methane to acetic acid in an aqueous medium. *Nature* **368**, 613–615 (1994).
4. Forster, D. Mechanistic pathways in the catalytic carbonylation of methanol by rhodium and iridium complexes. *Adv. Organomet. Chem.* **17**, 255–267 (1979).
5. Periana, R. A., Mironov, O., Taube, D., Bhalla, G. & Jones, C. Catalytic, oxidative condensation of CH_4 to CH_3COOH in one step via C-H activation. *Science* **301**, 814–818 (2003).
6. Zheng, K. et al. Room-temperature photooxidation of CH_4 to CH_3OH with nearly 100% selectivity over hetero-ZnO/Fe_2O_3 porous nanosheets. *J. Am. Chem. Soc.* **144**, 12357–12366 (2022).
7. Qi, G. et al. Au-ZSM-5 Catalyses the selective oxidation of CH_4 to CH_3OH and CH_3COOH using O_2. *Nat. Catal.* **5**, 45–54 (2022).
8. Mohamedali, M., Ayodele, O. & Ibrahim, H. Challenges and prospects for the photocatalytic liquefaction of methane into oxygenated hydrocarbons. *Renew. Sust. Energ. Rev.* **131**, 110024 (2020).
9. Hammond, C. et al. Direct catalytic conversion of methane to methanol in an aqueous medium by using copper-promoted Fe-ZSM-5. *Angew. Chem. Int. Ed.* **51**, 5129–5133 (2012).
10. Snyder, B. E. R. et al. The active site of low-temperature methane hydroxylation in iron-containing zeolites. *Nature* **536**, 317–321 (2016).
11. Sushkevich, V. L., Palagin, D., Ranocchiari, M. & van Bokhoven, J. A. Selective anaerobic oxidation of methane enables direct synthesis of methanol. *Science* **356**, 523–527 (2017).
12. Lieberman, R. L. & Rosenzweig, A. C. Crystal structure of a membrane-bound metalloenzyme that catalyses the biological oxidation of methane. *Nature* **434**, 177–182 (2005).
13. Yu, B. et al. Silver and copper dual single atoms boosting direct oxidation of methane to methanol via synergistic catalysis. *Adv. Sci.* **10**, 2302143 (2023).
14. Zhang, Q. et al. Establishing metal-nonoxygen bonds to improve thermal stability of Pt_1/CeO_2 via coating boron nitride. *Chem. Eng. Sci.* **302**, 120856 (2025).
15. Ni, L. et al. Thiourea modification promoting the activity on Pt/CeO_2 for CO oxidation by weakening the metal–support interaction. *Ind. Eng. Chem. Res.* **64**, 4835–4844 (2025)
16. Yu, B. et al. Surface hydroxyl group dominating aerobic oxidation of methane below room temperature. *Energy Environ. Sci.* **17**, 8127–8139 (2024).
17. Zhao, Y. et al. Steric-confinement Rh_2/MoS_2 dual-atom catalyst directionally modulating adsorption configuration of ester group to boost ethanol synthesis. *Chem* **10**, 3342–3363 (2024).
18. Shi, Y. et al. Local In-O-Pd lewis acid-base pair boosting CO_2 selective hydrogenation to methanol. *Chem. Eng. J.* **485**, 150093 (2024).
19. Zhou, P. et al. Synergetic interaction between neighboring platinum and ruthenium monomers boosts CO oxidation. *Chem. Sci.* **10**, 5898–5905 (2019).

20. Zhao, Q.-P. et al. Photo-induced synthesis of heteronuclear dual-atom catalysts. *Nat. Synth.* **3**, 497–506 (2024).
21. Chen, J. et al. Photoinduced precise synthesis of diatomic Ir_1Pd_1-In_2O_3 for CO_2 hydrogenation to methanol via angstrom-scale-distance dependent synergistic catalysis. *Angew. Chem. Int. Ed.* **63**, e202401168 (2024).
22. Zeng, M. et al. ZSM-5-confined Cr_1–O_4 active sites boost methane direct oxidation to C1 oxygenates under mild conditions. *EES Catal.* **1**, 153–161 (2023).
23. Wang, S. et al. H_2-reduced Phosphomolybdate promotes room-temperature aerobic oxidation of methane to methanol. *Nat. Catal.* **6**, 895–905 (2023).
24. Zhao, Y. et al. Vacancy defects inductive effect of asymmetrically coordinated single-atom Fe—N_3S_1 active sites for robust electrocatalytic oxygen reduction with high turnover frequency and mass activity. *Adv. Mater.* **36**, 2308243 (2024).
25. Ou, H. et al. Carbon nitride photocatalysts with integrated oxidation and reduction atomic active centers for improved CO_2 conversion. *Angew. Chem. Int. Ed.* **61**, e202206579 (2022).
26. Wang, G. et al. Bonding interaction of adjacent Pt and Ag single-atom pairs on carbon nitride efficiently promotes photocatalytic H_2 production. *CCS Chem.* **6**, 1523–1534 (2024).
27. An, Z. et al. Highly active, Ultra-low loading single-atom iron catalysts for catalytic transfer hydrogenation. *Nat. Commun.* **14**, 6666 (2023).
28. Cui, J. et al. Regulating the metal–support interaction: double jump to reach the efficiency apex of the Fe–N_4-catalyzed fenton-like reaction. *ACS Catal.* **12**, 14954–14963 (2022).
29. Zhang, X. et al. Identifying and tailoring C–N coupling site for efficient urea synthesis over diatomic Fe–Ni catalyst. *Nat. Commun.* **13**, 5337 (2022).
30. Zhang, L. et al. Water activation triggered by Cu-Co double-atom catalyst for silane oxidation. *Angew. Chem. Int. Ed.* **62**, e202313343 (2023).
31. Shu, X., Tan, D., Wang, Y., Ma, J. & Zhang, J. Bimetal-bridging nitrogen coordination in carbon-based electrocatalysts for pH-universal oxygen Reduction. *Angew. Chem. Int. Ed.* **63**, e202316005 (2024).
32. Yang, Y. et al. Integrating enrichment, reduction, and oxidation sites in one system for artificial photosynthetic diluted CO_2 reduction. *Adv. Mater.* **35**, 2304170 (2023).
33. Su, H. et al. Flexibility tuning of dual-metal S-Fe-Co-N_5 catalysts with O-axial ligand structure for electrocatalytic water splitting. *Adv. Energy Mater.* **13**, 2301547 (2023).
34. Li, Y. et al. Synergistic effect of atomically dispersed Ni–Zn pair sites for enhanced CO_2 electroreduction. *Adv. Mater.* **33**, 2102212 (2021).
35. Sun, X. et al. Isolated Fe-Co heteronuclear diatomic sites as efficient bifunctional catalysts for high-performance lithium-sulfur batteries. *Nat. Commun.* **14**, 291 (2023).
36. Li, L. et al. Efficient sunlight-driven dehydrogenative coupling of methane to ethane over a Zn^+-modified zeolite. *Angew. Chem. Int. Ed.* **50**, 8299–8303 (2011).
37. Cheng, M. et al. Constructing charge transfer channel between dopants and oxygen vacancies for enhanced visible-light-driven water oxidation. *Nano. Res.* **14**, 3365–3371 (2021).
38. Yan, Y., Jiang, S., Zhang, H. & Zhang, X. Preparation of novel Fe-ZSM-5 zeolite membrane catalysts for catalytic wet peroxide oxidation of phenol in a membrane reactor. *Chem. Eng. J.* **259**, 243–251 (2015).
39. Yasin, G. et al. Simultaneously engineering the synergistic-effects and coordination-environment of dual-single-atomic iron/cobalt-sites as a bifunctional oxygen electrocatalyst for rechargeable zinc-air batteries. *ACS Catal.* **13**, 2313–2325 (2023).
40. Lu, W. et al. Preparation of ZnO films with variable electric field-assisted atomic layer deposition technique. *Appl. Surf. Sci.* **303**, 111–117 (2014).
41. Kong, Y. et al. Atomically dispersed Zinc(I) active sites to accelerate nitrogen reduction kinetics for ammonia electrosynthesis. *Adv. Mater.* **34**, 2103548 (2022).
42. Deng, D. et al. Engineering electronic density and coordination environment of Mn-N_x sites via Zn cooperation for quasi-solid-state zinc-air batteries. *Renewables* **1**, 362–372 (2023).
43. Qiao, B. et al. Highly efficient catalysis of preferential oxidation of CO in H_2-Rich stream by gold single-atom catalysts. *ACS Catal.* **5**, 6249–6254 (2015).
44. Tsukamoto, D. et al. Photocatalytic H_2O_2 production from ethanol/O_2 system using TiO_2 loaded with Au–Ag bimetallic alloy nanoparticles. *ACS Catal.* **2**, 599–603 (2012).
45. Ruschel, G. K., Nemetz, T. M. & Ball, D. W. Matrix isolation and density functional studies of novel transition metal complexes. NO + Fe, Co, Ni, Cu, and Zn in argon matrices. *J. Mol. Struct.* **384**, 101–114 (1996).
46. Sun, J., Gao, W., Fei, H. & Zhao, G. Efficient and selective electrochemical reduction of nitrate to N_2 by relay catalytic effects of Fe-Ni bimetallic sites on MOF-derived structure. *Appl. Catal. B Environ.* **301**, 120829 (2022).
47. Wang, L. et al. In situ DRIFTS study of the NO + CO reaction on Fe–Co binary metal oxides over activated semi-coke supports. *RSC Adv.* **7**, 7695–7710 (2017).
48. Snyder, B. E. R. et al. Mechanism of selective benzene hydroxylation catalyzed by iron-containing zeolites. *Proc. Natl. Acad. Sci. USA* **115**, 12124–12129 (2018).
49. Kumar, M. S., Schwidder, M., Grünert, W. & Brückner, A. On the nature of different iron sites and their catalytic role in Fe-ZSM-5 DeNOx catalysts: new insights by a combined EPR and UV/VIS spectroscopic approach. *J. Catal.* **227**, 384–397 (2004).
50. Yu, T. et al. Highly selective oxidation of methane into methanol over Cu-promoted monomeric Fe/ZSM-5. *ACS Catal.* **11**, 6684–6691 (2021).
51. Wang, H. et al. Facilitating the dry reforming of methane with interfacial synergistic catalysis in an Ir@CeO_{2-x} catalyst. *Nat. Commun.* **15**, 3765 (2024).
52. Li, M. et al. Single-step selective oxidation of methane to methanol in the aqueous phase on iridium-based catalysts. *Appl. Catal. B Environ.* **292**, 120124 (2021).
53. Alexander, A. J., Kim, Z. H. & Zare, R. N. Photodissociation of O_2 via the herzberg continuum: measurements of O-atom alignment and orientation. *J. Chem. Phys.* **118**, 10566–10574 (2003).
54. Buijsse, B. et al. Angular distributions for photodissociation of O_2 in the herzberg continuum. *J. Chem. Phys.* **108**, 7229–7243 (1998).
55. Zare, R. N. & Herschbach, D. R. Doppler line shape of atomic fluorescence excited by molecular photodissociation. *P. IEEE* **51**, 173–182 (1963).
56. Kepp, K. P. A quantitative scale of oxophilicity and thiophilicity. *Inorg. Chem.* **55**, 9461–9470 (2016).
57. Xu, J., Cao, X.-M. & Hu, P. Improved prediction for the methane activation mechanism on rutile metal oxides by a machine learning model with geometrical descriptors. *J. Phys. Chem. C.* **123**, 28802–28810 (2019).
58. Aljama, H., Nørskov, J. K. & Abild-Pedersen, F. Theoretical insights into methane C–H bond activation on alkaline metal oxides. *J. Phys. Chem. C.* **121**, 16440–16446 (2017).
59. Szecsenyi, A., Li, G., Gascon, J. & Pidko, E. A. Mechanistic complexity of methane oxidation with H_2O_2 by single-site Fe/ZSM-5 catalyst. *ACS Catal.* **8**, 7961–7972 (2018).
60. Van Heuvelen, K. M. et al. One-electron oxidation of an oxoiron(IV) complex to form an $[O=Fe^{V}=NR]^+$ center. *Proc. Natl. Acad. Sci. USA* **109**, 11933–11938 (2012).
61. Nakamoto, K. Resonance raman spectra and biological significance of high-valent Iron (IV, V) porphyrins. *Coord. Chem. Rev.* **226**, 153–165 (2002).

62. Snyder, B. E. R. et al. Structural characterization of a non-heme iron active site in zeolites that hydroxylates methane. *Proc. Natl. Acad. Sci. USA* **115**, 4565–4570 (2018).
63. Hou, K. et al. Reactive high-spin iron(IV)-oxo sites through dioxygen activation in a metal–organic framework. *Science* **382**, 547–553 (2023).
64. Zhang, Y. et al. H_2O_2 Generation from O_2 and H_2O on a near-infrared absorbing porphyrin supramolecular photocatalyst. *Nat. Energy* **8**, 361–371 (2023).
65. Jin, Z. et al. Hydrophobic zeolite modification for in situ peroxide formation in methane oxidation to methanol. *Science* **367**, 193–197 (2020).
66. Xu, W. et al. Metal-oxo electronic tuning via in situ CO decoration for promoting methane conversion to oxygenates over single-atom catalysts. *Angew. Chem. Int. Ed.* **63**, e202315343 (2024).
67. Xie, J. et al. Stable photocatalytic coupling of methane to ethane with water vapor using TiO_2 supported ultralow loading AuPd nanoparticles. *Acta Phys. Sin.-Ch. Ed.* **39**, 2306037 (2023).
68. Wu, W. et al. CO_2 Hydrogenation over copper/ZnO single-atom catalysts: water-promoted transient synthesis of methanol. *Angew. Chem. Int. Ed.* **61**, e202213024 (2022).
69. Ding, L. et al. Over 70 % faradaic efficiency for CO_2 electroreduction to ethanol enabled by potassium dopant-tuned interaction between copper sites and intermediates. *Angew. Chem. Int. Ed.* **61**, e202209268 (2022).
70. Li, F.-M., Xia, C., Fang, W., Chen, Y. & Xia, B. Y. RhCuBi Trimetallenes with composition segregation coupled crystalline-amorphous heterostructure toward ethanol electrooxidation. *Adv. Energy Mater.* **14**, 2400112 (2024).
71. Jia, G. et al. Asymmetric coupled dual-atom sites for selective photoreduction of carbon dioxide to acetic acid. *Adv. Funct. Mater.* **32**, 2206817 (2022).
72. Liu, Y., Xue, D., Li, W., Li, C. & Wan, B. A simple method for the precise determination of multi-elements in pyrite and magnetite by ICP-MS and ICP-OES with matrix removal. *Microchem. J.* **158**, 105221 (2020).
73. Kresse, G. & Hafner, J. Ab initio molecular dynamics for liquid metals. *Phys. Rev. B* **47**, 558–561 (1993).
74. Perdew, J. P. et al. Atoms, molecules, solids, and surfaces: applications of the generalized gradient approximation for exchange and correlation. *Phys. Rev. B* **46**, 6671–6687 (1992).
75. Perdew, J. P., Burke, K. & Ernzerhof, M. Generalized gradient approximation made simple. *Phys. Rev. Lett.* **77**, 3865–3868 (1996).
76. Grimme, S., Ehrlich, S. & Goerigk, L. Effect of the damping function in dispersion corrected density functional theory. *J. Comput. Chem.* **32**, 1456–1465 (2011).
77. Cheng, Q. et al. Maximizing active Fe species in ZSM-5 zeolite using organic-template-freesynthesis for efficient selective methane oxidation. *J. Am. Chem. Soc.* **145**, 5888–5898 (2023).
78. Dauenhauer, P. J. & Abdelrahman, O. A. A universal descriptor for the entropy of adsorbed molecules in confined Spaces. *ACS Cent. Sci.* **4**, 1235–1243 (2018).

Acknowledgements

This project was supported financially by the National Key R&D Program of China (2021YFB3501900, 2023YFA1507601), National Natural Science Foundation of China (U21A20326, 22172065, 22306063, and 22022302), Natural Science Foundation of Jiangsu Province (BK20211239), and Jiangsu Specially-Appointed Professor (1046010241211400). We thank the Center for High Performance Computing at Shanghai Jiao Tong University for providing the computing resources of the Siyuan-1 cluster. We acknowledge support from Lixia Yan (Analysis and Testing Center of Jiangnan University) for the help with the HRTEM/STEM test.

Author contributions

Baiyang Yu: Data curation, Investigation, Formal analysis, Writing-original draft. Wenlong Li: DFT Data curation, Investigation, Formal analysis, Writing-original draft. Xuan Tang: Data curation, Investigation, Formal analysis. Lu Cheng: DFT Data curation, Investigation, Formal analysis. Fudong Liu: Data curation, Investigation, Formal analysis. Jiawei Zhang: Formal analysis. Shuobing Yang: Formal analysis. Jing Xu: Formal analysis. Ying Zhang: Investigation. Chengsi Pan: Formal analysis. Xiaoming Cao: DFT Data curation, Supervision, Writing-review & editing. Yongfa Zhu: Supervision. Yang Lou: Conceptualization, Methodology, Data curation, Funding acquisition, Writing-original draft, review & editing.

Competing interests

The authors declare no competing interests.

Additional information

Supplementary information The online version contains supplementary material available at https://doi.org/10.1038/s41467-025-64505-9.

Correspondence and requests for materials should be addressed to Xiao-Ming Cao or Yang Lou.

Peer review information *Nature Communications* thanks the anonymous reviewer(s) for their contribution to the peer review of this work. A peer review file is available.